

Article

Multi-Objective Optimization of a Solar Combined Power Generation and Multi-Cooling System Using CO₂ as a Refrigerant

Rania Hammemi ^{1,*}, Mouna Elakhdar ¹, Bourhan Tashtoush ² and Ezzedine Nehdi ¹

¹ Research Laboratory Energetic and Environment, National Engineering School of Tunis (ENIT), Tunis El Manar University, Tunis 1002, Tunisia

² Mechanical Engineering Department, Jordan University of Science and Technology (JUST), Irbid 22110, Jordan

* Correspondence: raniahammeme75@yahoo.com

Abstract: This paper proposes a new combined multi-cooling and power generation system (CMCP) driven by solar energy. Carbon dioxide is used as a refrigerant. A parabolic trough collector (PTC) is employed to collect solar radiation and convert it into thermal energy. The system includes a supercritical CO₂ power system for power production and an ejector refrigeration system with two ejectors to provide cooling at two different evaporating temperatures. The CMCP system is simulated hourly with weather conditions for Tunisia. The PTC mathematical model is used to calculate the heat transfer fluid outlet temperature and the performance of the CMCP system on a specific day of the year. A 1D model of an ejector with a constant area is adopted to evaluate the ejector performance. The system's performance is evaluated by an energetic and exergetic analysis. The importance of the system's components is determined by an exergoeconomic analysis. The system is modeled using MATLAB software. A genetic algorithm is used for multi-objective optimization to determine the best values and solutions for the system's design parameters. The optimal energy and exergy efficiencies were found to be 13.7 percent and 37.55 percent, respectively, and the total product unit cost was 31.15 USD/GJ.

Keywords: combined system; CO₂ power cycle; multi-cooling; ejector; exergoeconomic analysis; multi-objective optimization



Citation: Hammemi, R.; Elakhdar, M.; Tashtoush, B.; Nehdi, E. Multi-Objective Optimization of a Solar Combined Power Generation and Multi-Cooling System Using CO₂ as a Refrigerant. *Energies* **2023**, *16*, 1585. <https://doi.org/10.3390/en16041585>

Academic Editors: Taskin Jamal, Josep M. Guerrero, GM Shafiullah and Md. Nasimul Islam Maruf

Received: 4 January 2023

Revised: 30 January 2023

Accepted: 1 February 2023

Published: 4 February 2023



Copyright: © 2023 by the authors. Licensee MDPI, Basel, Switzerland. This article is an open access article distributed under the terms and conditions of the Creative Commons Attribution (CC BY) license (<https://creativecommons.org/licenses/by/4.0/>).

1. Introduction

According to estimates from the International Energy Agency, between 1973 and 2015, the world's energy consumption increased by more than 200% [1]. The challenges related to energy use and carbon emissions are also becoming more crucial. To solve these problems, scientists have been attempting to increase efficiency through the integration of various energy systems, as well as the use of renewable energy sources, including solar, wind, and hydroelectric power. In contrast to non-renewable resources such as fossil fuels, which have a limited supply and contribute to climate change and pollution by releasing greenhouse gases, renewable energy sources are plentiful, can be regenerated over time, and have a less negative environmental impact. Using integrated cooling and power systems, often known as cogeneration systems, is one technique to improve energy efficiency and minimize greenhouse gas emissions. Combined systems can generate electricity from a variety of fuels, including natural gas, biomass, and waste heat, all of which are typically more sustainable and cleaner than coal or oil [2]. Combined systems have proven to be an effective approach to save energy, save money, and reduce pollutants [3].

Numerous academics have been drawn to the integration of power cycles to use waste heat in industrial operations and available renewable energy [4,5]. Power cycles could use biomass [6], geothermal [7], and ocean thermal energy [8]. Furthermore, power systems can effectively be used in combination with different cycles [9], the internal combustion

engine [10], and heavy-duty diesel engine applications [11]. They can also be used in combined heat and power systems [12], combined power and refrigeration systems, [13], and combined cooling, heating, and power systems [14]. These combinations successfully utilize waste heat in power generation cycles and highly enhance the system's energy efficiency.

For the power sub-cycle of cogeneration systems, the organic Rankine cycle [15], carbon dioxide (CO₂) [16], and Kalina cycles [17] are usually employed, whereas the refrigeration sub-cycles used are frequently the absorption refrigeration [18] and ejector cooling cycles [19].

Research has looked into how well a solar-powered refrigeration and power system performs. Renewable energy applications, among others, have drawn further attention to ejector technology [20,21]. Solar ejector cooling cycles are commonly used in air conditioning systems [22,23] because the cooling effect can be created while generating power using an ORC [24]. These cycles have numerous advantages, including dependability, simplicity, and minimal operational and installation costs, and they can employ a variety of refrigerants. Additionally, the ORC was incorporated into ECC to create electrical power and a refrigerating effect. Exergy and parametric analyses were performed to evaluate the new design of a co-generation system for power and cold, and operating parameters were modified to improve the system's exergy efficiency [15,25]. Another cycle configuration was studied, and the system performance was evaluated with the refrigerant R245fa. The results of the simulation showed that the ejector had the maximum exergy losses [26]. Renewable solar energy was utilized in a tri-generation system to produce power, heating, and cooling. Several refrigerants were studied to select the one with the best performance [27,28]. In another work, an ejector 1D unsteady model was presented, and a theoretical analysis was carried out to estimate the system performance with different refrigerants [29]. A combined ECC with the Kalina cycle for cooling and power generation was investigated and analyzed [30,31]. Exergy and exergoeconomic analysis have been largely applied for evaluating and optimizing various energy conversion processes. An energetic and exergetic analysis of three novel combined power systems and ECC was proposed [32]. This study aimed to improve the performance of the basic combined power and ECC performance by suggesting three novel cycles and comparing their performance [32]. Another exergetic study was carried out to investigate the performance of a combined power plant using a high-temperature energy storage system with a solar parabolic trough [33]. An exergoeconomic analysis of an absorption chiller integrated with an ORC using parabolic trough collectors was performed. The authors found that the average cost of exergy of the power generated was about USD 12 per GJ [34]. The exergetic efficiency and overall capital cost were selected as the main two functions to ensure maximum exergy efficiency and lower capital cost in the power-generating cycle [35]. In another study, three functions were used to find the best refrigerant to be used in an ORC [36]. A multi-objective optimization was also presented for a trigeneration solar system to find the maximum average output power with a minimum heat input [24,37]. Thermodynamic and economic analysis of a combined trigeneration solar ECC system was presented using the exergy costing method [38]. Exergy, energy, environmental, and economic analyses were carried out to study the combined tri-generation cycle performance. The authors used an algorithm for cycle optimization by having the levelized cost at a minimum value with a maximum value of exergy efficiency [39]. An ECC driven by the waste heat of exhaust gases was investigated and an exergoeconomic analysis was conducted with system optimization using MATLAB Software [40]. The authors optimized the cycle by combining the minimum product cost with maximum exergy efficiency. Recently, a novel combined system of ECC and ORC for application in space-cooling was presented. Two different working fluids, Isobutane and Toluene, were used in the ECC and ORC, and the source heat was the excess heating of the exhaust gases and the rejected heat from the ORC condenser. The exergy efficiency and relative annual benefit functions were used for the system's optimization. The output cooling capacity was 271.1 kW and the ORC system generated 225.6 kW of electrical power

with 26.2% thermal efficiency [41]. The genetic algorithms (GA) were implemented in multi-objective optimization since they can ensure an accurate and robust approach. A small-scale solar-driven ORC was optimized by a GA to minimize the payback period and increase the exergy efficiency. Different types of solar collectors and working fluids were evaluated for the weather conditions of the Mediterranean [42]. Lately, a theoretical analysis was conducted to evaluate the system's performance by developing a mathematical model of a parabolic trough collector (PTC) system of a combined ORC with ECC. The objective of the work was to determine and control the temperatures of the glass cover of the PTC receiver, absorber, and working fluid [43]. According to the literature review, several factors have a significant impact on system performance from a thermodynamic, economic, and environmental standpoint; as a result, single-objective optimization was unable to accurately assess how well the performance of the combined systems performed. This should be urgently carried out to perform multi-objective optimization.

The previously mentioned research demonstrates that multi-generation systems, such as cogeneration and trigeneration systems, are desirable choices that can improve energy generation performance and address many related dependability, safety, and flexibility issues. In this regard, a variety of prime mover technologies are available, and the decision amongst them depends heavily on the circumstances and preferences of the end user [44]. There are several ways to address major energy and environmental issues, such as improving the efficiency of power generation systems and using waste heat and renewable energy as heat sources. The supercritical CO₂ cycle, which utilizes highly dense and thermally conductive CO₂ as a working fluid, has been proposed as a potential solution to these challenges [45–47]. This approach may offer several benefits due to the properties of supercritical CO₂. The supercritical power CO₂ cycle uses carbon dioxide as a working fluid, and it has several advantages over traditional steam Rankine cycles and gas Brayton cycles. One of these advantages is the ability to operate at higher turbine inlet temperatures, since CO₂ is less corrosive at high temperatures than steam. Additionally, the supercritical CO₂ cycle requires less compression work and has more compact heat exchangers and turbines, which can result in lower costs and higher efficiency [48]. The supercritical CO₂ cycle is compatible with a wide range of heat sources, particularly renewable energy, and it is also used in combined cooling, power, and heating systems [49]. Over the years, various configurations of the supercritical CO₂ cycle have been developed, making it an increasingly promising technology for power generation [50,51].

In the present work, a new solar combined multi-cooling and power generation (CMCP) system using CO₂ is proposed. The CMCP system consists of a parabolic trough solar collector (PTC) as the heat supply to the system, a supercritical CO₂ power system for power production, and two ejector refrigeration systems for cooling supply at two different evaporating temperatures. CO₂ is used as the working fluid. An energetic analysis of the CMCP system is conducted to evaluate its performance under Tunisian weather conditions. Owing to the importance of the system simulation over time, the hourly simulation of the solar cogeneration system is conducted. The PTC mathematical model is used to calculate the heat transfer fluid (HTF) outlet temperature and the solar cogeneration system's performance on a particular day of the year. The proposed system is modeled using MATLAB software, and the equations of mass and energy are implemented to develop the computer program. An exergetic analysis is conducted to evaluate the system's thermodynamic performance. The system's component exergetic efficiency and destruction rates are determined. The importance of the comparative cost of each component is found by conducting the exergoeconomic analysis since it includes not only the bare module cost (BMC), operation and maintenance costs (OMC), and fuel cost, but also the exergy destruction costs within the component. The system's economic analysis is based on the total revenue requirement (TRR) method of the system. The multi-objective optimization to determine the ideal values and solution of the system's design parameters is performed using a genetic algorithm (GA). Total product unit cost (TPUC) and exergetic efficiency are

the system's objective optimization functions. For multi-objective optimization with GA, the MATLAB software's optimization toolbox is used.

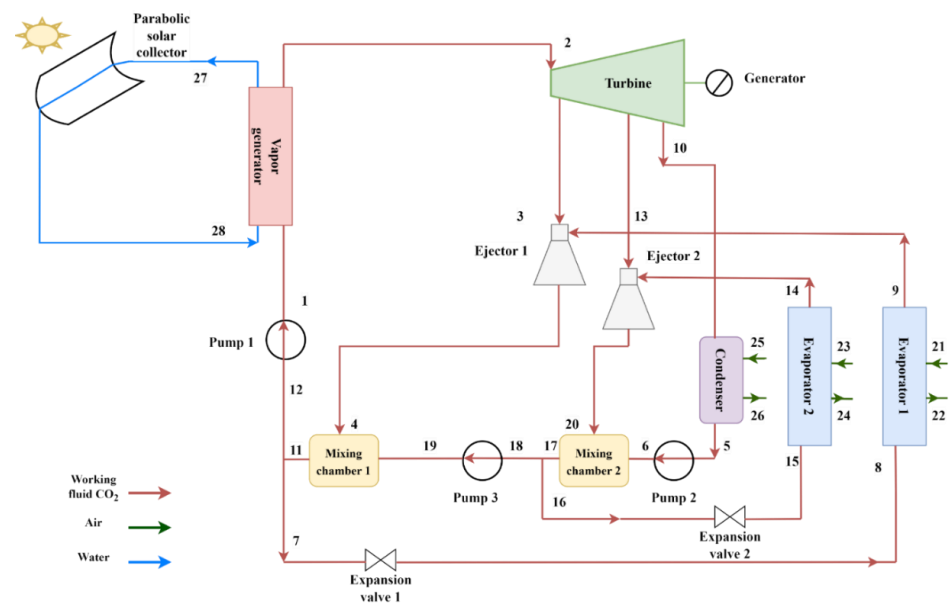
The next sections of this article are organized as follows. Section 2 describes the studied system. Sections 3–6 discuss the energetic, exergetic, economic, and exergoeconomic analysis of the system. Section 7 defines the principle of the multi-objective optimization adopted in the article. Section 8 examines the base case results. Section 9 covers the parametric study of key parameters of the system. Section 10 examines the optimization results. The paper ends with a conclusion (Section 11) that includes a summary of the research.

2. The System's Description

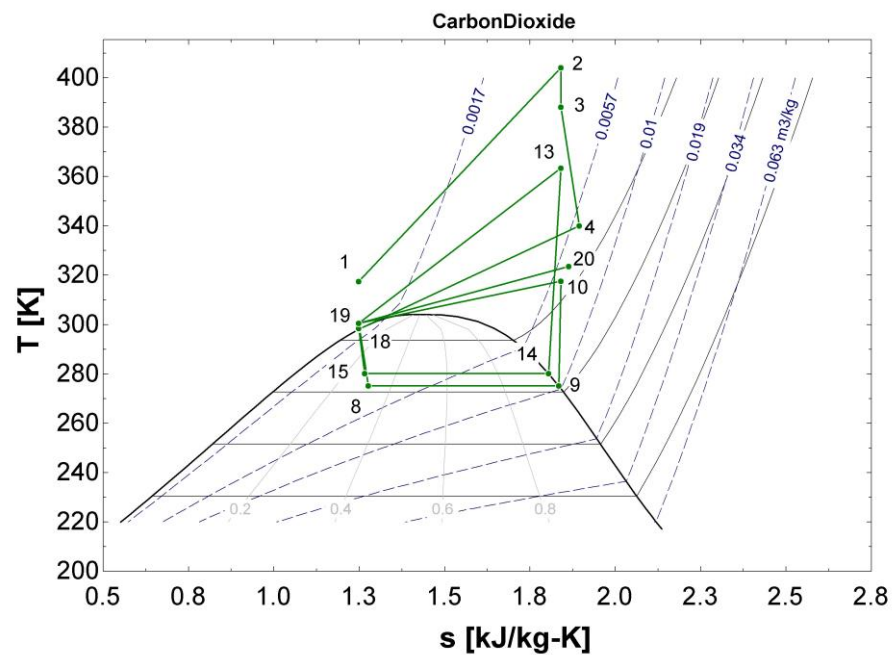
The schematic diagram of the solar combined multi-cooling and power generation system is shown in Figure 1a. Figure 1b depicts the new system's T-s diagram. The system's primary components are the parabolic trough solar collector, in which the heat transfer fluid (HTF) circulates, the supercritical CO₂ power system, and the CO₂ ejector refrigeration system.

In summary, the process described involves heating supercritical CO₂ in the generator so that high pressure and temperature are achieved (state 2), and then introducing this heated carbon dioxide into the turbine to be expanded with isentropic expansion, resulting in the production of power. At the steam generator, the CO₂ at high pressure and temperature is generated by the absorption of heat from the solar collector. At the turbine, there will be two extractions, and therefore two quantities of CO₂ will enter the two ejectors. Primary fluid, or the extracted CO₂ from the turbine, passes via the drive nozzle of the ejector. For both ejectors, the vapor removed from the turbine (states 3 and 13) is mixed with the vapor leaving the evaporators (states 9 and 14) in a mixing chamber inside the ejector before being compressed in the diffuser. Between the turbine's extraction pressure and the evaporation pressure, a new pressure is created (states 4 and 20). The condenser condenses the fully expanded vapor leaving the turbine (state 10) to state 5. Then, the condensate passes through the second pump (state 6), where it is mixed with the steam leaving the second ejector in the mixing chamber (state 20). The liquid, assumed to be in a saturated state (state 17), leaving the second mixing chamber is pumped to state 19 and then mixed with the vapor leaving the first ejector (state 4). The fluid at state 16 is expanded through the second expansion valve. The liquid assumed to be in a saturated state (state 11) is partially compressed and sent to the steam generator through pump 1. The fluid at state 7 is expanded through the first expansion valve. At low pressure and temperature, the liquid enters the evaporator (states 8 and 15) and produces a cooling effect.

The (T, S) diagram is given in Figure 1b. It shows the different isentropic and isothermal evolutions of the studied system. The CMCP consists of a parabolic trough solar collector (PTC), a supercritical CO₂ power system for power production (states 1, 2, 3, 13, and 10), and two-ejector refrigeration systems for cooling supply (states 4, 5, 6, 7, 8, 9, 11, 12, 14, 15, 16, 17, 18, 19, and 20).



(a)



(b)

Figure 1. (a) Schematic of the CMCP system. (b) The T-s diagram of the CMCP cycle.

3. The System's Energetic Analysis

The mathematical models of the solar-powered CMCP system mainly consist of the solar collector (PTC) model, the ejector model, and the CMCP model.

The following assumptions are used to simplify the calculations:

1. Heat transfer between machinery, pipes, and the environment is disregarded, and the system is steady.
2. Heat exchangers and pipe pressure drops are ignored.
3. When the primary and secondary flows enter the ejector, they are both saturated vapor.
4. There is no heat loss as the ejector operates in a constant condition.
5. The isenthalpic evolution in the expansion valve.

6. Constant isentropic efficiency for the turbine and pump are 90% and 80%, respectively.
7. The ambient reference temperature and pressure are 25 °C and 1 atm, respectively.
8. The steam generator efficiency is assumed to be 0.5.
9. The entrainment ratio of ejector 1 and ejector 2 is assumed to be 0.3 and 0.45, respectively.

The energy and mass conservation principles are used to develop a computer program. Table 1 shows the energy balances for each component of the system.

$$\sum \dot{m}_{in} - \sum \dot{m}_{out} = 0 \tag{1}$$

$$\sum (\dot{m}h)_{in} - \sum (\dot{m}h)_{out} + \sum \dot{Q}_{in} - \sum \dot{Q}_{out} + \dot{W} = 0 \tag{2}$$

Table 1. Energy balances for the system components.

Component	Equation
Evaporator 1	$\dot{Q}_{e1} = \dot{m}_9 * (h_9 - h_8)$
Evaporator 2	$\dot{Q}_{e2} = \dot{m}_{14} * (h_{14} - h_{15})$
Condenser	$\dot{Q}_{cond} = \dot{m}_{10} * (h_{10} - h_5)$
Expansion valve 1	$h_8 = h_7$
Expansion valve 2	$h_{16} = h_{15}$
Ejector 1	$\dot{m}_4 * h_4 = \dot{m}_3 * h_3 + \dot{m}_9 * h_9$
Ejector 2	$\dot{m}_{20} * h_{20} = \dot{m}_{14} * h_{14} + \dot{m}_{13} * h_{13}$
Pump 1	$\dot{W}_{p1} = \dot{m}_1 * (h_1 - h_{12})$
Pump 2	$\dot{W}_{p2} = \dot{m}_6 * (h_6 - h_5)$
Pump 3	$\dot{W}_{p3} = \dot{m}_{19} * (h_{19} - h_{18})$
Turbine	$\dot{W}_{turb} = \dot{m}_2 * (h_2 - h_3) + (\dot{m}_2 - \dot{m}_3) * (h_3 - h_{13}) + (\dot{m}_2 - \dot{m}_3 - \dot{m}_{13}) * (h_{13} - h_{10})$
Steam generator	$\dot{Q}_{ger} = \dot{m}_2 * (h_2 - h_1)$
Mixing chamber 1	$\dot{m}_{11} * h_{11} = \dot{m}_4 * h_4 + \dot{m}_{19} * h_{19}$
Mixing chamber 2	$\dot{m}_{17} * h_{17} = \dot{m}_6 * h_6 + \dot{m}_{20} * h_{20}$

The system’s thermal efficiency is calculated to evaluate the thermodynamic performance of the system. It is given as [43]:

$$\eta_{thermal} = \frac{\dot{W}_{Net} + \dot{Q}_{e1} + \dot{Q}_{e2}}{\dot{Q}_{ger}} \tag{3}$$

With

$$\dot{W}_{Net} = \dot{W}_{Turb} - (\dot{W}_{p1} + \dot{W}_{p2} + \dot{W}_{p3}) \tag{4}$$

3.1. PTC Modeling

One of the most well-known types of solar collectors is the parabolic trough collector (PTC), where a parabolic curved surface is lined with a receiver of a polished reflective metal mirror. The PTC collector is chosen for the proposed CMCP system to absorb solar radiation and convert it into thermal energy.

The water-based heat transfer fluid (HTF), a glass, and an absorber pipe make up the PTC collector. As the HTF moves through the absorber tube, the heat is transferred. The glass shell that surrounds the tube allows solar radiation to enter while also minimizing heat exchange with the surroundings and reducing infrared radiation losses. The HTF circulates inside the absorber tube, where its temperature is increased due to heat transfer from sun radiation. The energy balances shown in Figure 2 are used to simulate the HTF outlet temperature.

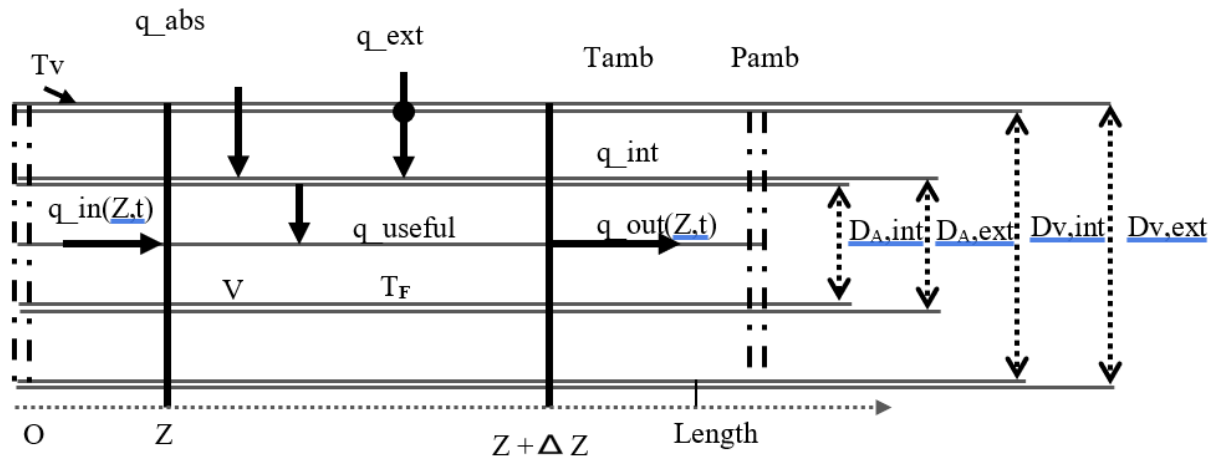


Figure 2. The PTC surface element thermal balance.

The collector’s energy from the sun is represented by the variable q_{abs} . The heat transmission from the absorber pipe’s interior surface to the fluid is q_{useful} .

$q_{int,convection}$ measures the convective heat transfer between the glass envelope and the absorber.

$q_{int,conduction}$ represents the heat transmission through the absorber by conduction.

Between the sky and the glass container, $q_{ext,radiation}$ represents the heat transfer by radiation. $q_{ext,convection}$ is the convective heat transfer between the atmosphere and the glass envelope. Between the glass container and the absorber, $q_{int,radiation}$ represents the radiation heat transfer.

The collector’s energy from the sun is represented by the variable q_{abs} .

The HTF energy balance can be represented as follows:

$$\rho_F C_F A_{A,int} \frac{\partial T_F(z,t)}{\partial t} = q_{in}(z,t) - q_{out}(z + \Delta z) + q_{useful}(z,t) \Delta z \tag{5}$$

Equation (3) has the following initial and boundary conditions:

$$T_F(0,t) = T_{F,in}(t) = T_{amb}(t)$$

$$T_F(z,0) = T_{F,initial}(z) = T_{amb}(0)$$

Newton’s law of cooling is used to estimate the absorber pipe’s interior surface convective heat gain as follows:

$$q_{useful} = h_F A_{A,int} (T_A - T_F) \tag{6}$$

According to [52], the absorbed thermal energy by the collector is approximately:

$$q_{abs} = W_{eff} \gamma_{interception} (\rho \tau \alpha \beta) I_G \tag{7}$$

The following formula determines the interception factor based on G_i , I_G , and C :

$$\gamma_{interception} = \frac{I_G(\beta)}{G_i(\beta)} + \frac{1}{C} \left(1 - \frac{I_G(\beta)}{G_i(\beta)} \right) \tag{8}$$

where, G_i , I_G , and C are the global and direct irradiation and the concentration factor, respectively.

3.2. Ejector Modeling

The ejector schematic diagram is shown in Figure 3. It consists of two coaxial nozzles. The driving nozzle is made by a convergent and a diverging nozzle, and the secondary

nozzle is constructed by a convergent section; a cylindrical part called the mixer and a diffuser.

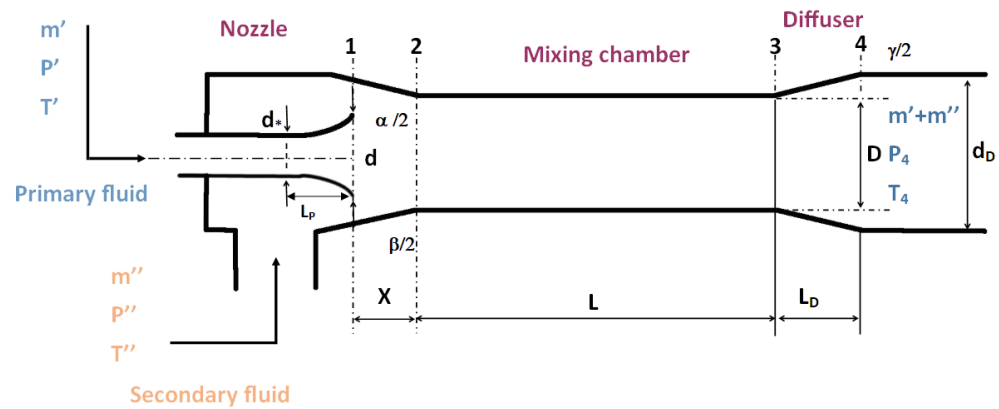


Figure 3. Schematic of the ejector.

The secondary flow, which has a lower energy level, meets the primary flow, which has high energy levels and stagnation pressure, close to the motor nozzle’s exit. The two fluids engage in interaction within the mixing chamber. The diffuser converts most of the kinetic energy of this flow into pressure energy at the outflow. Depending on the conditions of operation, three different flow regimes can exist in the ejector. The relationship between the pressure at the ejector outlet and the mass flow rate ratio between the secondary flow and the primary flow is what gives rise to the names of these three flow regimes. Supersonic, transitional, and mixed regimes are these three conditions.

The ejector models, on the other hand, are divided into two groups based on the nozzle position and various assumptions made for the mixing of the fluids, depending on whether the mixing of the main and secondary fluids occurs at constant pressure or in a mixing chamber with a constant cross-section [40,53,54]. The ejector’s performance is influenced by geometrical and thermodynamic parameters. According to various studies, the transition regime provides the best ejector performances [55–57]. Table 2 defines the various geometrical and thermodynamic parameters of the ejector.

Table 2. The geometrical and thermodynamic parameters of the ejector.

Geometrical parameters	φ	The ratio of the cross-sectional area at the outlet of the primary nozzle and the cross-sectional area at the throat of the primary nozzle = $\left(\frac{d}{d_*}\right)^2$
	Ω	The ratio of the cross-sectional area at the outlet of the secondary nozzle and the cross-sectional area at the throat of the mixing chamber = $\left(\frac{d_p}{D}\right)^2$
	ϕ	The ratio of the mixing chamber cross-section and the cross-section at the throat of the driving nozzle = $\left(\frac{D}{d_*}\right)^2$
	(X/d)	The relative positioning of the primary nozzle.
	(L/D)	The relative length of the mixing chamber.
	L_p/d	The relative length of the divergent part of the primary nozzle.
Thermodynamic parameters	(L_D/D)	The relative length of the divergent part of the secondary nozzle.
	α, β, γ	Angles of the convergent and divergent primary and secondary nozzles.
	$U = m''/m'$	The ejector entrainment ratio, U
	P'/P''	The expansion ratio, Γ
	P_4/P''	The compression ratio, r
	P'/P_4	The driving pressure ratio, ξ

The geometric parameters, ϕ , X/D , and L/D , as well as the thermodynamic parameters U , ξ , Γ , and r , are the most influential [55,57]. A previous study on ejectors has been targeted

at optimizing their role and searching for suitable operating points involving specified relationships with these parameters.

To apply to the CMCP running with CO₂, the ejector is modeled in a transition regime with a 1D constant area [55].

Some assumptions are made for the analysis as follows:

1. An ideal gas working fluid with constant thermal conductivity, k , and heat-specific heat capacity, C_p .
2. Steady flow inside the ejector.
3. Before mixing, the isentropic relations are utilized for simplicity in the 1D model.
4. The two liquids are completely blended when they leave the mixing chamber.

When the distance X is not equal to zero, the flow in the convergent part is supersonic, and the aerodynamic throat is located in the cylindrical part of the mixing chamber. Based on this information, we can deduce that:

$$M_2'' = 1 \quad (9)$$

$$\left[1 + U\theta^{\frac{1}{2}}\right] [f_3(M_3) + xM_3] = f_3(M_2') + 2U\theta^{\frac{1}{2}} \quad (10)$$

$$f_2(k, M_4) = \frac{f_2(k, M_3)}{\eta_D \Omega} \quad (11)$$

$$f_2(k, M_4) = f_4(k, M_4) \xi \frac{1 + U\theta^{\frac{1}{2}}}{\Phi \Omega} \quad (12)$$

$$U\theta^{\frac{1}{2}} = \frac{1}{\Gamma} \left[\Phi - \frac{1}{f_2(k, M_2')} \right] \quad (13)$$

$$\Gamma = \left(\frac{2}{k+1} \right)^{\frac{k}{k-1}} \frac{1}{f_4(k, M_2')} \quad (14)$$

In which:

$$f_2(k, M) = \left(\frac{k+1}{2} \right)^{\frac{1}{k-1}} M \left(1 - \frac{k-1}{k+1} M^2 \right)^{\frac{1}{k-1}} \quad (15)$$

$$f_3(M) = M + \frac{1}{M} \quad (16)$$

$$f_4(k, M) = \left(1 - \frac{k-1}{k+1} M^2 \right)^{\frac{k}{k-1}} \quad (17)$$

$$\eta_D = \frac{P_4}{P_3} \quad (18)$$

$$\theta = \frac{T''}{T'} \quad (19)$$

The obtained governing equations are solved using a consecutive substitution and iteration method. The computational flowchart in the transition regime is shown in Figure 4.

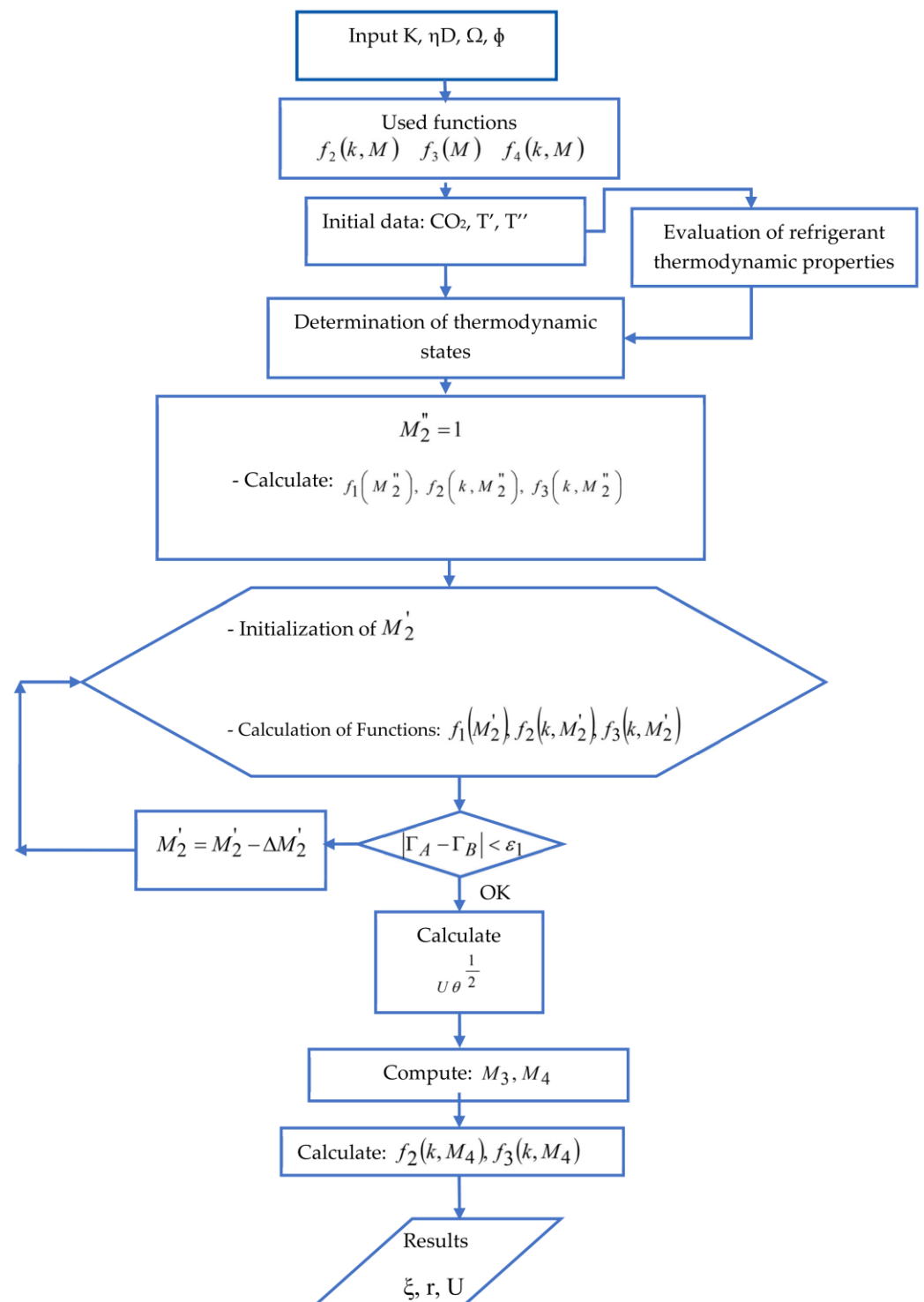


Figure 4. Ejector calculation flow chart.

4. The System's Exergetic Analysis

The energy balance places its emphasis on the quantity of energy rather than its quality. Exergy in thermodynamics describes the nature of a specific amount of energy.

Exergy, then, is the most theoretically possible useful work that may be obtained from an energy conversion system based on its conditions compared to the environmental balance, according to [58].

Additionally, energy analysis is an extension of exergy analysis. It considers the usable energy of a stream of energy capable of performing work. In comparison to energy analysis,

it offers a more precise examination of thermodynamic systems and can be carried out at the system, subsystem, or component level.

The majority of the system's overall exergy is composed of chemical, physical, potential, and kinetic exergy:

$$\dot{E}_{\text{tot}} = \dot{E}_{\text{ch}} + \dot{E}_{\text{ph}} + \dot{E}_{\text{pt}} + \dot{E}_{\text{kn}} \quad (20)$$

The physical exergy is calculated as follows:

$$\dot{E}_{\text{ph}} = \dot{m}[(h_i - h_0) - T_0(s_i - s_0)] \quad (21)$$

The temperature, enthalpy, and entropy are denoted by h , T , and s , respectively, and the given and reference states are denoted by the subscripts o and i , respectively.

The exergy of fuel and product (\dot{E}_F and \dot{E}_P) approach [58] is applied in the exergy analysis on the component and system levels. An exergy balance of the overall system is given in Equation (22), where the exergy destruction and losses are denoted by \dot{E}_D and \dot{E}_L , respectively.

$$\dot{E}_{F,\text{tot}} = \dot{E}_{P,\text{tot}} + \dot{E}_{D,\text{tot}} + \dot{E}_{L,\text{tot}} \quad (22)$$

Neglecting the rate of exergy loss of individual components, one can obtain:

$$\dot{E}_{F,k} = \dot{E}_{P,k} + \dot{E}_{D,k} \quad (23)$$

Exergetic efficiency ϵ_k is defined as the ratio

$$\epsilon_k = \frac{\dot{E}_{P,k}}{\dot{E}_{F,k}} \quad (24)$$

Overall system exergy efficiency ϵ_{tot}

$$\epsilon_{\text{tot}} = \frac{\dot{E}_{P,\text{tot}}}{\dot{E}_{F,\text{tot}}} \quad (25)$$

The exergy destruction ratio $y_{D,k}^*$

$$y_{D,k}^* = \frac{\dot{E}_{D,k}}{\dot{E}_{D,\text{tot}}} \quad (26)$$

Thermodynamic inefficiency should be calculated only for the mixer and condenser, since in these components, the destruction and transfer of exergy to the environment are accomplished without achieving any positive exergetic effect [59]. Table 3 shows the exergy balance equations of the system.

$$\dot{E}_{D,k, \text{dissipative}} = \dot{E}_{\text{in},k} - \dot{E}_{\text{out},k} \quad (27)$$

Table 3. Exergy balance equations.

Component	Exergy Fuel Rate ($\dot{E}_{F,k}$)	Exergy Product Rate ($\dot{E}_{P,k}$)
Evaporator 1	$\dot{E}_{F,e1} = \dot{E}_8 - \dot{E}_9$	$\dot{E}_{P,e1} = \dot{E}_{22} - \dot{E}_{21}$
Evaporator 2	$\dot{E}_{F,e2} = \dot{E}_{15} - \dot{E}_{14}$	$\dot{E}_{P,e2} = \dot{E}_{24} - \dot{E}_{23}$
Condenser	$\dot{E}_{F,\text{cond}} = \dot{E}_{10} - \dot{E}_5$	$\dot{E}_{P,\text{cond}} = \dot{E}_{26} - \dot{E}_{25}$
Expansion valve 1	$\dot{E}_{F,\text{ev1}} = \dot{E}_7$	$\dot{E}_{P,\text{ev1}} = \dot{E}_8$
Expansion valve 2	$\dot{E}_{F,\text{ev2}} = \dot{E}_{16}$	$\dot{E}_{P,\text{ev2}} = \dot{E}_{15}$
Ejector 1	$\dot{E}_{F,\text{eject1}} = \dot{m}_3 * (e_3 - e_4)$	$\dot{E}_{P,\text{eject1}} = \dot{m}_9 * (e_4 - e_9)$

Table 3. Cont.

Component	Exergy Fuel Rate ($\dot{E}_{F,k}$)	Exergy Product Rate ($\dot{E}_{P,k}$)
Ejector 2	$\dot{E}_{F,ejec2} = \dot{m}_{13} * (e_{13} - e_{20})$	$\dot{E}_{P,ejec2} = \dot{m}_{14} * (e_{20} - e_{14})$
Pump 1	$\dot{E}_{F,p1} = \dot{W}_{p1}$	$\dot{E}_{P,p1} = \dot{E}_1 - \dot{E}_{12}$
Pump 2	$\dot{E}_{F,p2} = \dot{W}_{p2}$	$\dot{E}_{P,p2} = \dot{E}_6 - \dot{E}_5$
Pump 3	$\dot{E}_{F,p3} = \dot{W}_{p3}$	$\dot{E}_{P,p3} = \dot{E}_{19} - \dot{E}_{18}$
Turbine	$\dot{E}_{F,turb} = \dot{E}_2 - \dot{E}_3 - \dot{E}_{13} - \dot{E}_{10}$	$\dot{E}_{P,turb} = \dot{W}_{turb}$
Steam generator	$\dot{E}_{F,ger} = \dot{E}_{27} - \dot{E}_{28}$	$\dot{E}_{P,ger} = \dot{E}_2 - \dot{E}_1$
Total system	$\dot{E}_{F,Total} = \dot{E}_{F,ger}$	$\dot{E}_{P,Total} = \dot{E}_{P,e1} + \dot{E}_{P,e2} + \dot{W}_{net}$

5. The System's Economic Analysis

To evaluate and cost-optimize an energy conversion system, an economic analysis is required. The total revenue requirement (TRR) method was used [58]. The project's costs with the minimum required return on investment were evaluated. The TRR is estimated yearly based on the estimation of the total capital investment with the assumption of economic, operating, financial, and market input parameters. An equivalent series of constant payments are adopted for the annual investment and operating and maintenance cost (OMC) to have them levelized.

The levelized TRR is the summation of carrying charges (CC_L) and the expenses of (FC_L) and (OMC_L).

$$TRR_L = CC_L + FC_L + OMC_L \quad (28)$$

The CC_L stands for "capital investment cost", which comprises income and other taxes, preferred stock, return on investment (ROI) for debt, and total capital recovery. The fixed capital investment (FCI) and the interest due on the investment make up the total capital investment costs (TCI).

$$TCI = FCI + \text{interest} \quad (29)$$

The FCI is determined by adding the service facilities, architectural work, and contingencies to the system's BMC.

$$FCI = BMC_{tot} + \text{service facilities} + \text{architectural work} + \text{contingencies} \quad (30)$$

Using cost-estimating charts, and functions' costs, the purchase equipment cost (PEC) was calculated as the first stage of calculating the TCI. The cost of the equipment procurement was modified by a power law as follows:

$$PEC_{new} = PEC_{known} \left(\frac{X_{new}}{X_{known}} \right)^\alpha \quad (31)$$

X_{new} represents the size of the approximating equipment costs (PEC_{new}), X_{known} represents the size of the known equipment costs (PEC_{known}), and α represents the size exponent [58]. The chemical engineering plant cost index (CEPCI) elements are used to compute the equipment costs for a certain reference year and adjust them for the analysis year. The projected equipment cost PEC_{new} must therefore be updated to the reference year. The analysis's reference year is 2021, with a CEPCI value of 776.3:

$$PEC_{ref} = PEC_{old} \left(\frac{CEPCI_{ref}}{CEPCI_{old}} \right) \quad (32)$$

where the subscript old denotes the year the equipment's cost was valid, and the subscript ref denotes the year it was intended to be acquired.

The specific type and qualities of the equipment must be taken into account as factors after determining the cost of purchasing it. The cost estimation method's last step was applying the module factor (F_{BM}) to account for installation expenses. The F_{BM} takes into account all components required for installing the equipment, including labor, piping, tools, accessories, and anything else that can be included in cost estimation charts.

BMC was used to compute the total direct costs, while a percentage of the total direct costs was used to calculate the indirect costs. Therefore, the FCI is the addition of the BMC of the system to 25% of BMC_{tot} considered as service facilities and architectural work, and 10% of BMC_{tot} considered as contingencies.

Estimation of funds allowance in the construction period was carried out by two installments over the two years with 60% and 40% of the FCI and interest. The TCI is the summation of the FCI and the estimated fund allowances. The capital recovery factor is calculated as follows:

$$CRF = \frac{i_{eff}(i_{eff} + 1)^n}{(i_{eff} + 1)^n - 1} \quad (33)$$

i_{eff} is the rate of interest, and n is the lifetime.

CC_L , FC_L , and OMC_L are determined as follows:

$$CC_L = TCI * CRF \quad (34)$$

$$FC_L = FC_0 * CELF = FC_0 * \frac{k_{FC}(1 - k_{FC}^n)}{1 - k_{FC}} * CRF \quad (35)$$

and

$$OMC_L = OMC_0 * CELF = OMC_0 * \frac{k_{OMC}(1 - k_{OMC}^n)}{1 - k_{OMC}} * CRF \quad (36)$$

With $k_{FC} = \frac{1 + r_{FC}}{1 + i_{eff}}$ and $k_{OMC} = \frac{1 + r_{OMC}}{1 + i_{eff}}$, where r_{FC} is the average inflation rate of FC_L and r_{OMC} is the average inflation rate of the OMC_L .

FC_0 , OMC_0 is the first-year costs of FC and OMC, respectively.

The exergoeconomic analysis's input is \dot{Z} , the cost rate associated with the investment and OMC. \dot{Z} could be the cost of the components or the total system, as shown below:

$$\dot{Z}_k = \dot{Z}_k^{CI} + \dot{Z}_k^{OM} = \frac{CC_L}{\tau} \frac{PEC_k}{\sum PEC_k} + \frac{OMC_L}{\tau} \frac{PEC_k}{\sum PEC_k} \quad (37)$$

$$\dot{Z}_{tot} = \sum \dot{Z}_k \quad (38)$$

6. The System's Exergoeconomic Analysis

The unique combination of economic and exergy analysis is referred to as exergoeconomic analysis. It is a powerful and useful tool to identify hidden costs associated with a system that cannot be identified using conventional exergy, energy, or cost analysis. The information obtained through exergoeconomic analysis leads to finding the system's stream costs. The approach of exergoeconomic is vital for a cost-effective design of a system [59].

For each component of the system:

$$\dot{C}_{P,k} = \dot{C}_{F,k} + \dot{Z}_k \quad (39a)$$

$$c_P \dot{E}_{P,k} = c_F \dot{E}_{F,k} + \dot{Z}_k \quad (39b)$$

where $c_F = \frac{\dot{C}_{F,k}}{\dot{E}_{F,k}}$ and product $c_P = \frac{\dot{C}_{P,k}}{\dot{E}_{P,k}}$.

The rate of cost of exergy destruction in the component is

$$\dot{C}_{D,k} = c_F \dot{E}_{D,k} \quad (40)$$

For the overall system

$$\dot{C}_{P,tot} = \dot{C}_{F,tot} + \dot{Z}_{tot} - \dot{C}_{L,tot} \quad (41a)$$

$$c_{P,tot} \dot{E}_{P,tot} = c_{F,tot} \dot{E}_{F,tot} + \dot{Z}_{tot} - \dot{C}_{L,tot} \quad (41b)$$

where $c_{F,tot} = \frac{\dot{C}_{F,tot}}{\dot{E}_{F,tot}}$ and $c_{P,tot} = \frac{\dot{C}_{P,tot}}{\dot{E}_{P,tot}}$ are the average total cost of fuel and product, respectively.

The cost rate of exergy destruction in the overall system is

$$\dot{C}_{D,tot} = c_{F,tot} \sum \dot{E}_{D,k} \quad (42)$$

The relative cost difference r_k and the exergoeconomic factor f_k can be calculated as:

$$r_k = \frac{c_{P,k} - c_{F,k}}{c_{F,k}} \quad (43)$$

$$f_k = \frac{\dot{Z}_k}{\dot{Z}_k + \dot{C}_{D,k}} \quad (44)$$

The detailed cost balance equation with the corresponding auxiliary and the cost of equipment equations are shown in Table 4. The development and implementation of these equations on the system's components lead to a linear system of equations. The solution of this system determines the needed cost flow rates of the system's components and the exergy unit cost for all exergy streams. Table 5 shows the exergoeconomic balance equations for the cycle.

Table 4. Cost balance equations for the system components.

Component	Cost Balance Equation	Auxiliary Equations	Estimation of PEC (USD ₂₀₂₁)
Evaporator 1	$\dot{C}_9 + \dot{C}_{22} = \dot{C}_{21} + \dot{C}_8 + \dot{Z}_{e1}$	$c_{21} = 0$, $c_8 = c_9$	$PEC_{e1} = 7400 * (\frac{A_{e1}}{10})^{0.6}$
Evaporator 2	$\dot{C}_{14} + \dot{C}_{24} = \dot{C}_{15} + \dot{C}_{23} + \dot{Z}_{e2}$	$c_{23} = 0$, $c_{15} = c_{14}$	$PEC_{e2} = 7400 * (\frac{A_{e2}}{10})^{0.6}$
Condenser	$\dot{C}_5 + \dot{C}_{26} = \dot{C}_{10} + \dot{C}_{25} + \dot{Z}_{cond}$	$c_{25} = 0$, $c_5 = c_{10}$	$PEC_{cond} = 7400 * (\frac{A_{cond}}{10})^{0.6}$
Expansion valve 1	$\dot{C}_8 = \dot{C}_7 + \dot{Z}_{ev1}$	$c_{11} = c_7$ $c_{11} = c_1$	$PEC_{ev1} = 280 * \dot{m}_7$
Expansion valve 2	$\dot{C}_{15} = \dot{C}_{16} + \dot{Z}_{ev2}$	$c_{17} = c_{16}$ $c_{17} = c_{19}$	$PEC_{ev2} = 280 * \dot{m}_{15}$
Ejector 1	$\dot{m}_9(c_{4,9}e_4 - c_9e_9)$ $= \dot{m}_3c_3(e_3 - e_4) + \dot{Z}_{ej1}$ $c_{4,9} = c_4 + \frac{\dot{m}_3}{\dot{m}_9}(c_4 - c_3)$	-	$PEC_{ej1} = 14,840 * (\frac{\dot{w}_{f1} * r_{p1}}{100})^{0.6}$
Ejector 2	$\dot{m}_{14}(c_{14,20}e_{20} - c_{14}e_{14})$ $= \dot{m}_{13}c_{13}(e_{13} - e_{20}) + \dot{Z}_{ej2}$ $c_{14,20} = c_{20} + \frac{\dot{m}_{13}}{\dot{m}_{14}}(c_{20} - c_{13})$		$PEC_{ej2} = 14,840 * (\frac{\dot{w}_{f2} * r_{p2}}{100})^{0.6}$
Pump 1	$\dot{C}_1 = \dot{C}_{12} + C_{w,p1} + \dot{Z}_{p1}$	$c_{w,p1} = c_{w,turb}$	$PEC_{p1} = 17,280 * (\frac{\dot{w}_{p1}}{10})^{0.37}$
Pump 2	$\dot{C}_6 = \dot{C}_5 + C_{w,p2} + \dot{Z}_{p2}$	$c_{w,p2} = c_{w,turb}$	$PEC_{p2} = 17,280 * (\frac{\dot{w}_{p2}}{10})^{0.37}$
Pump 3	$\dot{C}_{19} = \dot{C}_{18} + C_{w,p3} + \dot{Z}_{p3}$	$c_{w,p3} = c_{w,turb}$	$PEC_{p3} = 17,280 * (\frac{\dot{w}_{p3}}{10})^{0.37}$

Table 4. Cont.

Component	Cost Balance Equation	Auxiliary Equations	Estimation of PEC (USD ₂₀₂₁)
Turbine	$\dot{C}_2 + \dot{Z}_{turb} = \dot{C}_3 + \dot{C}_{13} + \dot{C}_{10} + C_{w,turb}$	$c_2 = c_3$ $c_2 = c_{13}$ $c_2 = c_{10}$	$PEC_{turb} = 222,170 * (\frac{W_{turb}}{1000})^{0.5}$
	$\dot{C}_{28} + \dot{C}_2 = \dot{C}_{27} + \dot{C}_1 + \dot{Z}_{ger}$	$c_{27} = \frac{\dot{Z}_{solarcollector}}{E_{F,ger}}$ $c_1 = c_2$	$PEC_{ger} = 7400 * (\frac{A_{ger}}{10})^{0.6}$
	$\dot{C}_{11} = \dot{C}_{19} + \dot{C}_4$		
	$\dot{C}_{17} = \dot{C}_{20} + \dot{C}_6$		

Table 5. Cost balance equations for the exergoeconomic analysis.

Component	Generated Product Rate ($\dot{C}_{P,k}$)	Fuel Supplied Rate ($\dot{C}_{F,k}$)	Exergy Destruction Rate ($\dot{C}_{D,k}$)
Evaporator 1	$\dot{C}_{P,e1} = \dot{C}_{22} - \dot{C}_{21}$	$\dot{C}_{F,e1} = \dot{C}_8 - \dot{C}_9$	$\dot{C}_{D,e1} = \dot{E}_{D,e1} * c_{F,e1}$
Evaporator 2	$\dot{C}_{P,e2} = \dot{C}_{24} - \dot{C}_{23}$	$\dot{C}_{F,e2} = \dot{C}_{15} - \dot{C}_{14}$	$\dot{C}_{D,e} = \dot{E}_{D,e2} * c_{F,e2}$
Condenser	$\dot{C}_{P,cond} = \dot{C}_{26} - \dot{C}_{25}$	$\dot{C}_{F,cond} = \dot{C}_{10} - \dot{C}_5$	$\dot{C}_{D,cond} = \dot{E}_{D,cond} * c_{F,cond}$
Expansion valve 1	$\dot{C}_{P,ev1} = \dot{C}_8$	$\dot{C}_{F,ev1} = \dot{C}_7$	$\dot{C}_{D,ev1} = \dot{E}_{D,ev1} * c_{F,ev1}$
Expansion valve 2	$\dot{C}_{P,ev2} = \dot{C}_{15}$	$\dot{C}_{F,ev2} = \dot{C}_{16}$	$\dot{C}_{D,ev2} = \dot{E}_{D,ev2} * c_{F,ev2}$
Ejector 1	$\dot{C}_{P,ejec1} = \dot{m}_9(c_{4,9}e_4 - c_9e_9)$	$\dot{C}_{F,ejec1} = \dot{m}_3c_3(e_3 - e_4)$	$\dot{C}_{D,ejec1} = \dot{E}_{D,ejec1} * c_{F,ejec1}$
Ejector 2	$\dot{C}_{P,ejec2} = \dot{m}_{14}(c_{14,20}e_{20} - c_{14}e_{14})$	$\dot{C}_{F,ejec2} = \dot{m}_{13}c_{13}(e_{13} - e_{20})$	$\dot{C}_{D,ejec2} = \dot{E}_{D,ejec2} * c_{F,ejec2}$
Pump 1	$\dot{C}_{P,pump1} = \dot{C}_1 - \dot{C}_{12}$	$\dot{C}_{F,pump1} = \dot{W}_{pump1} * c_{w,pump1}$	$\dot{C}_{D,pump1} = \dot{E}_{D,pump1} * c_{F,pump1}$
Pump 2	$\dot{C}_{P,pump2} = \dot{C}_6 - \dot{C}_5$	$\dot{C}_{F,pump2} = \dot{W}_{pump2} * c_{w,pump2}$	$\dot{C}_{D,pump2} = \dot{E}_{D,pump2} * c_{F,pump2}$
Pump 3	$\dot{C}_{P,pump3} = \dot{C}_{19} - \dot{C}_{18}$	$\dot{C}_{F,pump3} = \dot{W}_{pump3} * c_{w,pump3}$	$\dot{C}_{D,pump3} = \dot{E}_{D,pump3} * c_{F,pump3}$
Turbine	$\dot{C}_{P,turb} = \dot{W}_{Turb} * c_{w,Turb}$	$\dot{C}_{F,turb} = \dot{C}_2 - \dot{C}_{13} - \dot{C}_3 - \dot{C}_{10}$	$\dot{C}_{D,turb} = \dot{E}_{D,turb} * c_{F,turb}$
Steam generator	$\dot{C}_{P,ger} = \dot{C}_2 - \dot{C}_1$	$\dot{C}_{F,ger} = \dot{C}_{27} - \dot{C}_{28}$	$\dot{C}_{D,ger} = \dot{E}_{D,ger} * c_{F,ger}$
Total system	$\dot{C}_{P,tot} = \dot{C}_{P,e1} + \dot{C}_{P,e2} + \dot{C}_{Wnet}$	$\dot{C}_{F,tot} = \dot{C}_{F,ger}$	$\dot{C}_{D,tot} = \frac{\dot{C}_{F,tot}}{E_{F,tot}} * \dot{E}_{D,tot}$

7. Multi-Objective Optimization

In general, the nature of engineering problems has different objectives, which can be in conflict; however, they must be satisfied simultaneously. For these situations, a genetic algorithm is used to carry out a multi-objective optimization and to determine the optimal design parameters of the system. The genetic algorithm is a method of natural biological evolution to find the optimal solution [60]. A chaotic definition of numerous individuals is used as the primary population in the genetic algorithm. The adaptability of the individuals to the objective functions is the criterion of selection in each population. The selected individuals for the reproduction of a new population have high correspondence with objective functions. The main two operators in the optimization with the genetic algorithm are the cross-over and mutation. A cross-over operator is used to create offspring new chromosomes from the parent chromosomes' synthesis. The higher adaptability individuals have more chance to be chosen as parents, and the generated new population will gradually gain higher fitness to approach the optimal solution. The convergence process is guided by the cross-over operator [40].

Multi-objective optimization with GA was used to achieve the optimum solution. The optimization toolbox in MATLAB software was used for this purpose. The selected solver in the MATLAB software's optimization toolbox was the "Gamultiobj-multi-objective optimization using genetic algorithm". It uses the principle of the Non-dominated sorting genetic algorithm-II (NSGA-II) [61,62], which is an effective multi-objective optimization method.

Figure 5 depicts the GA optimization procedure and Table 6 summarizes the selected tuning parameters of the applied GA.

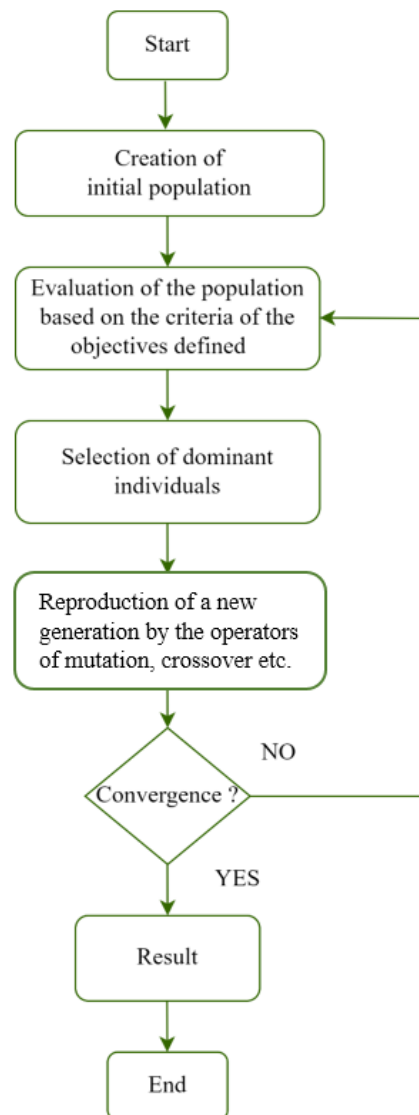


Figure 5. GA optimization procedure.

Table 6. The parameters of tuning in the GA program of optimization.

Parameters	Value
The size of the population	50
The generation maximum number	200
The selection function	Tournament
The size of the tournament	2
Probability of cross-over	95%
The function of mutation	Adaptive feasible
The function of cross-over	Intermediate

7.1. The Functions of Multi-Objective Optimization

The overall system optimization is achieved by implementing two essential objective functions, which are the exergetic efficiency that must be maximized and the cogeneration system's total product unit cost that has to be as low as possible. The following equations define these functions:

The first objective function is exergy efficiency:

$$\varepsilon_{\text{tot,cycle}} = \frac{\dot{E}_{P,e1} + \dot{E}_{P,e2} + \dot{W}_{\text{Net}}}{\dot{E}_{F,\text{ger}}} \quad (45)$$

In addition, the second objective function is the total product unit cost of the system:

$$\text{TPUC} = \frac{\dot{C}_{P,\text{tot}} + \dot{C}_{20}}{\dot{E}_{P,\text{tot}}} \quad (46)$$

7.2. The Decision Variables

The decision variables for the first cycle are the ratio of extraction, the secondary mass flow rate of the ejectors, the pressure of the steam generator, and the coefficient of evaporators, condenser, and steam generator. Table 7 lists the implemented ranges of these variables.

Table 7. The decision variables' range of the optimization of the system.

Parameters	Range
The ratio of extraction	[0.15; 0.33]
Secondary mass flow rate ejector 1 (\dot{m}_9)	[0.7; 1.2]
Secondary mass flow rate ejector 2 (\dot{m}_{14})	[0.7; 1.2]
Steam generator pressure (P_2)	[175; 200]
Evaporator 1 coefficient	[0.8; 1]
Condenser coefficient	[0.9; 1.2]
Evaporator 2 coefficient	[0.8; 1]
Steam generator coefficient	[1; 1.2]

8. Results and Discussion

8.1. Ejector Model Validation

The relevant data from the literature were used to validate the ejector model. Contrasting the outcomes of the simulation model of the ejector with those of a publicly available empirical correlation [63,64] validated the computer simulation program.

Additionally, based on the earlier experimental investigations of [63], this empirical correlation was developed for the performance prediction of ejectors in the optimal regime and irrespective of the fluid nature. Table 8 shows the strong concordance between the present findings and those obtained through the empirical correlation [63].

$$U = U_{\text{opt}} = 3.32 \left[\frac{1}{r} (1 - 1.21/\xi) \right]^{2.12} \quad (47)$$

Table 8. Ejector model validation.

	Ejector 1		Ejector 2	
	U	U_{Nehdi}	U	U_{Nehdi}
1	0.31	0.35	0.25	0.29
2	0.35	0.37	0.310	0.312
3	0.4	0.399	0.4	0.342

8.2. PTC Model Validation

The results given by [65] lend support to the PTC collector simulation model. They investigated the usage of a medium-temperature solar parabolic trough for cooling in Tunisia and assessed the system's thermal effectiveness and heat losses. The HTF circulating temperature in the PTC in the current investigation substantially resembles those noted [65], as seen in Figure 6.

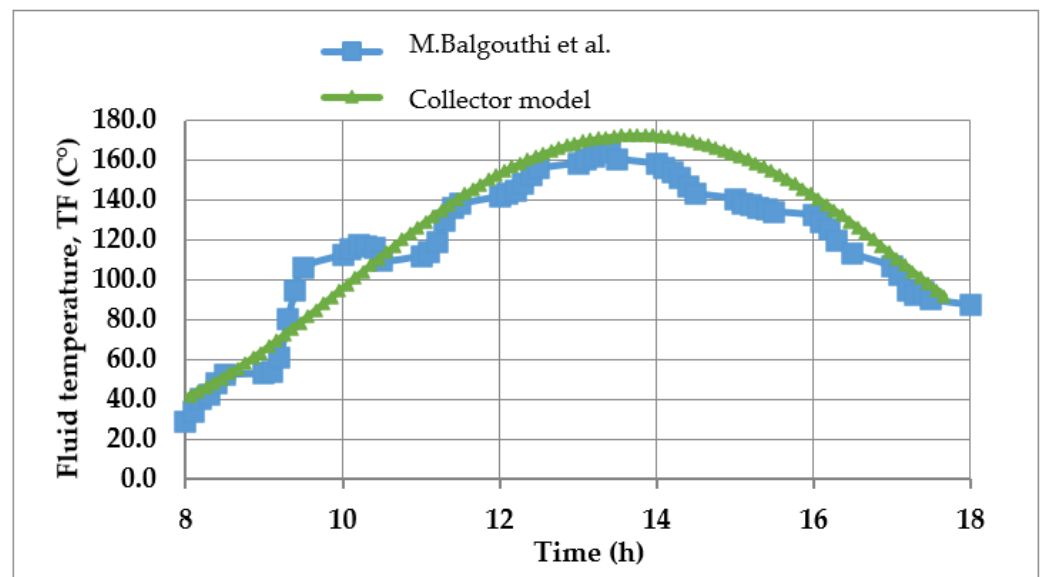


Figure 6. Validation of the PTC fluid temperature [65].

8.3. Overall Results

A MATLAB computer program was created to simulate the CMCP system. CO_2 thermodynamic properties were determined and calculated using the NIST and REFPROP databases [66]. The PTC simulation results were assessed hourly during an exemplary day. Figure 7 shows the hourly variation of the HTF temperature and global irradiance on 21 June, as estimated.

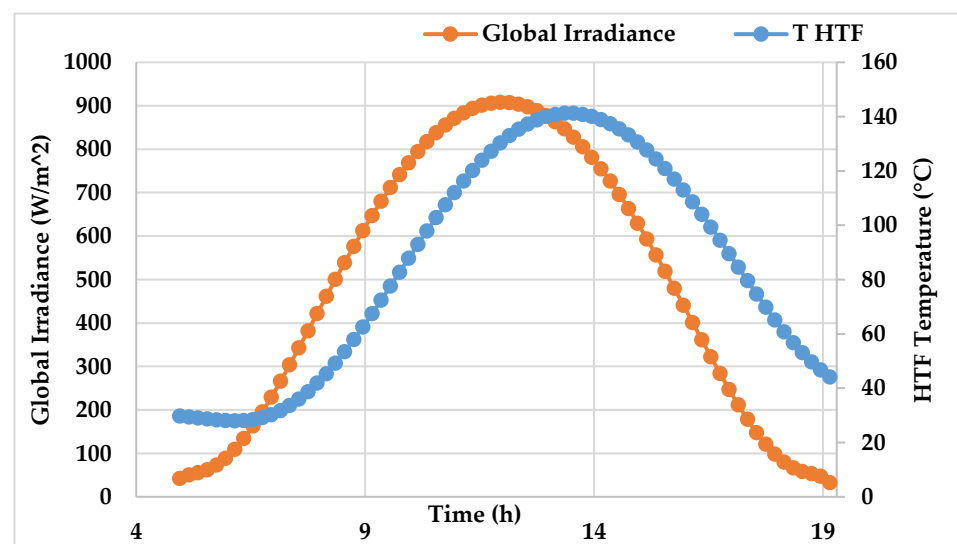


Figure 7. The HTF temperature and the global irradiance hourly variation, on 21 June.

The HTF hourly variation of temperature is affected by global irradiance. The incident heat energy is absorbed by the HTF and transferred to the refrigerant. The greatest temperature generated by the HTF is 141 °C between 01:00 and 03:00 p.m.

As illustrated in Figure 8, the HTF hourly temperature change in the PTC was used to visualize the energy performance of the CMCP system. Table 9 describes the system simulation's operating parameter settings. The largest net power output was achieved in the time interval of 01:00 and 3:00 p.m., as shown in Figure 8, because the highest produced temperature of the HTF was reached at the same time. Furthermore, the heat generated by

the steam generator reaches its peak. As a result, energy efficiency and net power output have an inverse relationship.

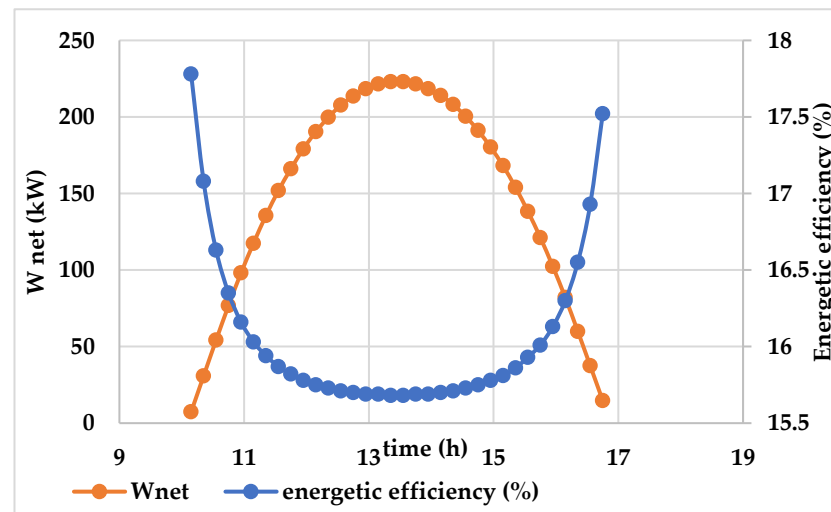


Figure 8. Hourly variation in energy efficiency and net power output.

Table 9. Operating conditions for the base case.

Parameters	Value
Evaporator temperature (°C)	2
Evaporator temperature (°C)	7
The difference in temperature (°C)	10
Steam generator temperature (°C)	131
Steam generator pressure (bar)	180
Condenser temperature (°C)	25
Expansion ratio 1	1.2
Expansion ratio 2	1.6
Extraction ratio 1	0.2
Ejector 1 secondary mass flow rate \dot{m}_9	0.9
Ejector 2 secondary mass flow rate \dot{m}_{14}	0.9
Pumps isentropic efficiency	0.8
Turbine isentropic efficiency	0.9
Ejector 1 entrainment ratio, U_1	0.3
Ejector 2 entrainment ratio, U_2	0.45

The simulation results of the CMCP system were evaluated on June 21st, at 1.55 p.m. The thermodynamic, exergetic, and exergoeconomic aspects at all the state points of the cycle using CO₂ were computed using the computer program. Tables 10 and 11 show the main performance indicators, thermodynamic and exergetic properties, as well as the unit cost of exergy flow at the various state points of the proposed system.

Table 10. The indicators of the solar-based cogeneration system performance.

Parameters	Value
Net power output (kW)	222.1
Cooling production (kW)	274
Heat power of the steam generator (kW)	3160
Energy efficiency (%)	15.69
Exergy efficiency (%)	31.65
Total product unit cost, USD/GJ	48.40

Table 11. Thermodynamic properties and stream costs.

	T	P	m	H	S	e	\dot{E}	c	\dot{C}
	[K]	[bar]	[kg·s ⁻¹]	[kJ·kg ⁻¹]	[kJ·(kg·K) ⁻¹]	[kJ·kg ⁻¹]	[kW]	(USD/GJ)	(USD/h)
1	317.45	180	15	290.04	1.25	228.69	3430.3	15.54	191.79
2	404.15	180	15	500.84	1.84	263	3945	13.99	198.59
3	388.24	150	3	491.11	1.84	253.27	759.82	13.99	38.248
4	339.95	74.635	3.9	476.93	1.89	222.95	869.49	17.22	53.856
5	298.15	64.342	10	274.78	1.25	213.43	2134.3	13.99	107.44
6	298.5	65.758	10	274.98	1.25	213.62	2136.2	14.28	109.71
7	300.53	74.635	0.9	276.22	1.25	214.86	193.38	15.54	10.812
8	275.15	36.733	0.9	276.22	1.28	206.56	185.9	16.24	10.86
9	275.15	36.733	0.9	429.65	1.83	193.73	174.36	16.24	10.186
10	317.62	64.342	10	452.71	1.84	214.87	2148.7	13.99	108.16
11	300.53	74.635	15.9	276.22	1.25	214.86	3416.3	15.54	191.01
12	300.53	74.635	15	276.22	1.25	214.86	3222.9	12.99	150.63
13	363.48	112.5	2	476.98	1.84	239.14	478.27	13.99	24.076
14	280.15	41.765	0.9	425.81	1.80	198.8	178.92	15.22	9.7983
15	280.15	41.765	0.9	274.98	1.27	208.5	187.65	15.22	10.276
16	298.5	65.758	0.9	274.98	1.25	213.62	192.26	14.79	10.228
17	298.5	65.758	12.9	274.98	1.25	213.62	2755.8	14.79	146.59
18	298.5	65.758	12	274.98	1.25	213.62	2563.5	14.19	130.83
19	300.53	74.635	12	276.22	1.25	214.86	2578.3	14.79	137.16
20	323.51	65.758	2.9	461.1	1.86	216.3	627.26	16.35	36.887
21	285	1	27.458	411.21	3.84	0.30061	8.254	0.00	0
22	280	1	27.458	406.18	3.82	0.57935	15.908	51.35	2.9385
23	290	1	26.987	416.24	3.86	0.11416	3.0808	0.00	0
24	285	1	26.987	411.21	3.84	0.30061	8.1127	93.16	2.7186
25	298	1	589.35	424.29	3.88	0	0	0.00	0
26	301	1	589.35	427.31	3.89	0.013621	8.0278	326.23	9.4206
27	414.15	3.7189	15.421	593.45	1.75	76.381	1177.9	1.18	4.9915
28	365.8	3.7189	15.421	388.42	1.22	28.275	436.04	1.18	1.8478

Table 10 shows that the proposed CMCP system has a cooling capacity of 274 kW and a net power production of 222.1 kW. Using these outputs, the energy and exergy efficiencies are 15.7% and 31.65%, respectively. Furthermore, the product’s unit cost is estimated to be 48.40 USD/GJ.

Additionally, Figures 9 and 10 exhibit schematic representations of each component’s exergetic destruction rate and exergetic efficiency.

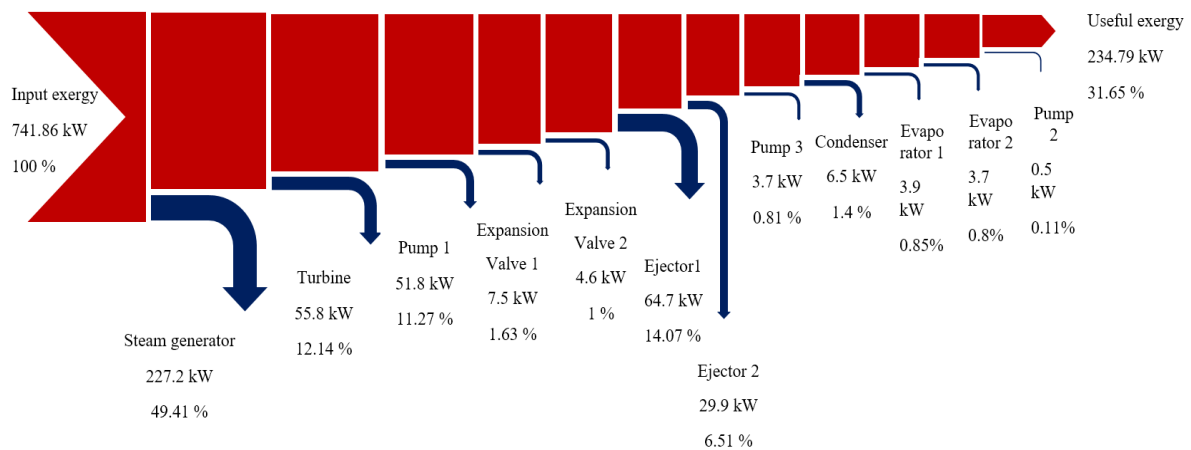


Figure 9. The exergy destruction within the group of productive and dissipative system’s components, kW.

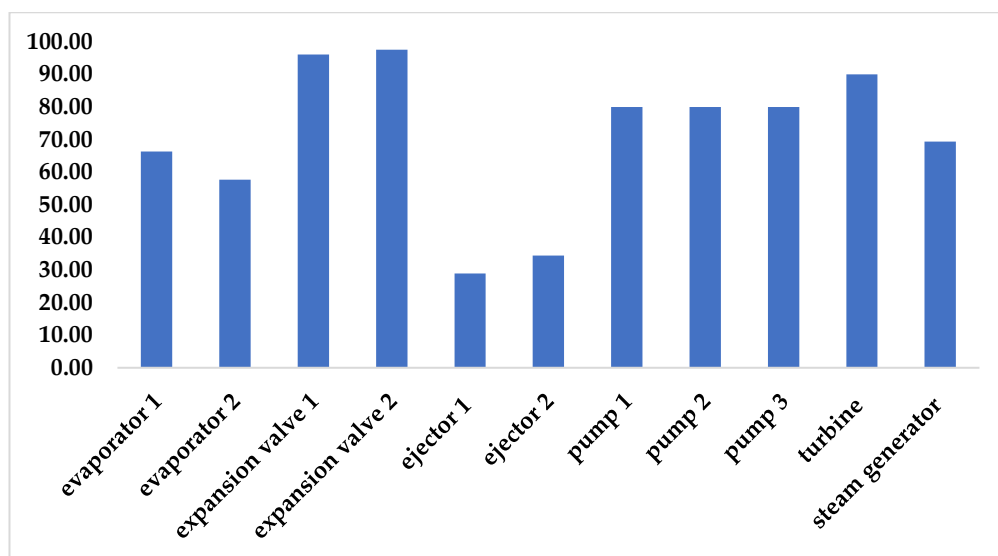


Figure 10. Product components' exergetic efficiency, %.

According to Figure 9, the component steam generator has the highest exergy destruction ratio of around 49.41%, with a corresponding exergy destruction rate of about 227.2 kW. The first ejector follows with a 64.7 kW exergy destruction rate and a 14.07% exergy destruction ratio. The turbine succeeds with a 55.8 kW exergy destruction rate and a 12.14% exergy destruction ratio.

Figure 10 also includes the exergy efficiency of each component in the proposed cogeneration system. The second expansion valve in the entire system has the highest exergy efficiency of up to 97.60%. The turbine is then followed by the first expansion valve. The first ejector had the lowest exergetic efficiency. Except for the ejector, the exergy efficiency of producing components is quite good, with an overall system average of 31.6%.

Some characteristics and assumptions are utilized to carry out the economic analysis for the proposed cycle. The parameters used are shown in Table 12. Table 13 shows the values of the fuel exergy cost rate, product exergy cost rate, exergy destruction cost rate, average component cost of fuel and product, exergoeconomic factor, and cost of each component for the basic input conditions. The component turbine has the highest cost of around 30.23 USD/h, followed by the first pump at 11.06 USD/h, and the condenser at 8.69 USD/h, while expansion valves have the lowest cost of about 0.05 USD/h. The second pump had the highest exergoeconomic factor at 97.17%, followed by the condenser and second evaporator at 96.40% and 91.73%, respectively.

Table 12. Assumptions and parameters of the economic analysis.

Assumptions/Parameters	Value
Plant life span	15 years
Interest rate	12%
CRF	0.147
The average inflation rate of the operating and maintenance cost, r_{OMC}	2.5%
CELF	1.165
Full load operational time τ , annually	7000 h

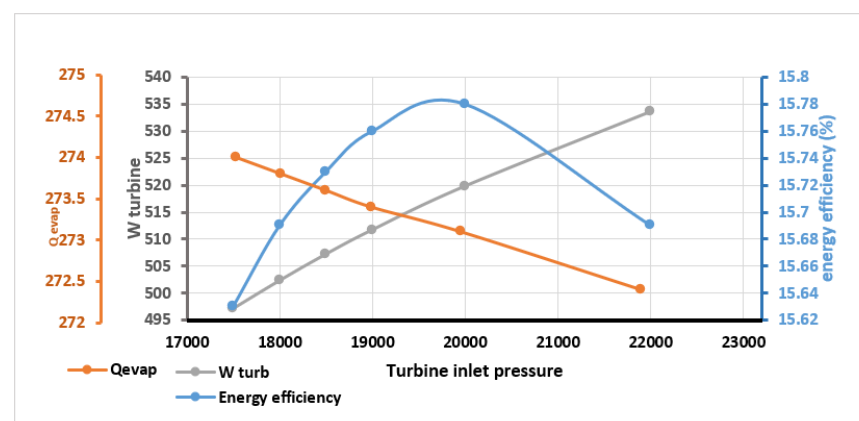
Table 13. Exergoeconomic parameters of the cycle.

Component	$\dot{C}_{P,k}$ (USD/h)	$\dot{C}_{F,k}$ (USD/h)	$c_{P,k}$ (USD/GJ)	$c_{F,k}$ (USD/GJ)	$\dot{C}_{D,k}$ (USD/h)	\dot{Z}_k (USD/h)	f_k (%)
Evaporator 1	2.94	0.67	106.73	16.24	0.23	2.26	90.88
Evaporator 2	2.72	0.48	150.20	15.22	0.20	2.24	91.73
Condenser	9.42	0.73	327.15	13.99	0.33	8.69	96.40
Expansion valve 1	10.86	10.81	16.24	15.54	0.42	0.05	10.37
Expansion valve 2	10.28	10.23	15.22	14.79	0.25	0.05	16.48
Ejector 1	10.00	4.58	105.75	13.99	3.26	5.42	62.47
Ejector 2	5.31	2.30	93.81	13.99	1.51	3.01	66.65
Pump 1	41.16	30.10	55.18	32.28	6.02	11.06	64.76
Pump 2	2.27	0.29	317.43	32.28	0.06	1.98	97.17
Pump 3	6.32	2.15	118.45	32.28	0.43	4.17	90.64
Turbine	58.33	28.10	32.28	13.99	2.81	30.23	91.50
Steam generator	6.79	3.14	3.67	1.18	0.96	3.65	79.12
Total	31.40	3.14	48.40	1.17	1.94	72.83	97.41

9. Parametric Study of Key Parameters

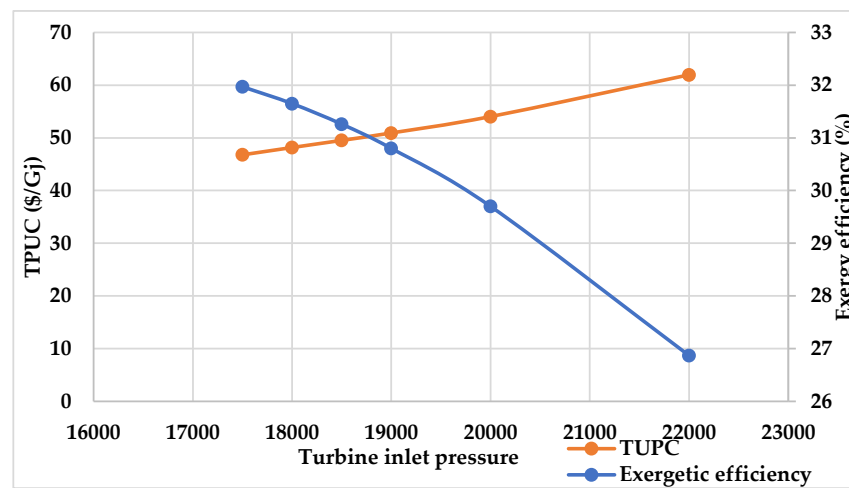
To show the suggested system's applicability, a parametric analysis of its thermodynamic and exergoeconomic performance metrics is carried out, and the way how different major assumed parameters affect the overall cycle performance is investigated.

Figure 11a,b depict the effect of inlet turbine pressure on the system's net main performance indicators. This pressure has a substantial impact on cycle performance. The graph illustrates that the rate of power generation increases. As a result, energy efficiency has a declining tendency, and exergy efficiency is always decreasing. Similarly, the overall unit cost of the product rises. In other words, increasing the turbine input pressure might increase the enthalpy difference through the turbine, resulting in increased turbine power. Meanwhile, the initial rise in energy efficiency is related to an increase in turbine power output, which compensates for the lower cooling generation rate. At higher pressures, however, the fall in cooling generation rate is accompanied with a considerable decrease, resulting in a decrease in energy efficiency. Because net electricity generated has the greatest impact on exergy efficiency, the exergy efficiency is decreasing.



(a)

Figure 11. Cont.

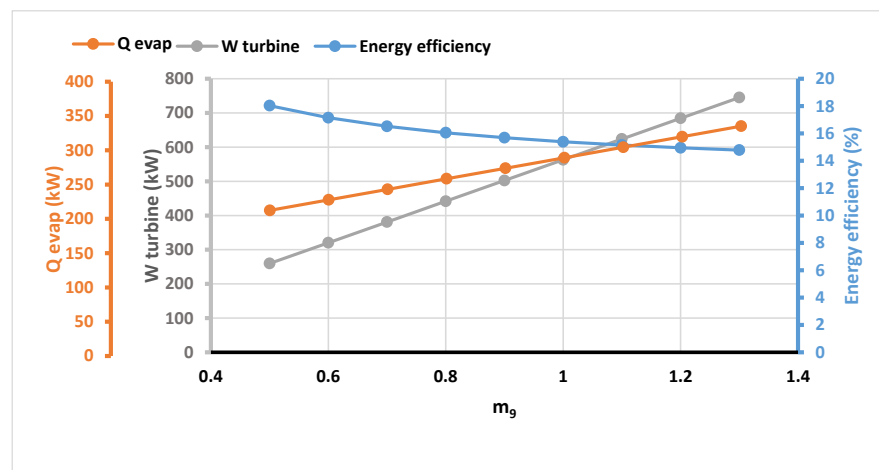


(b)

Figure 11. (a) Effect of turbine inlet pressure on energy efficiency, cooling, and power generation. (b) Effect of turbine inlet pressure on exergy efficiency and TPUC.

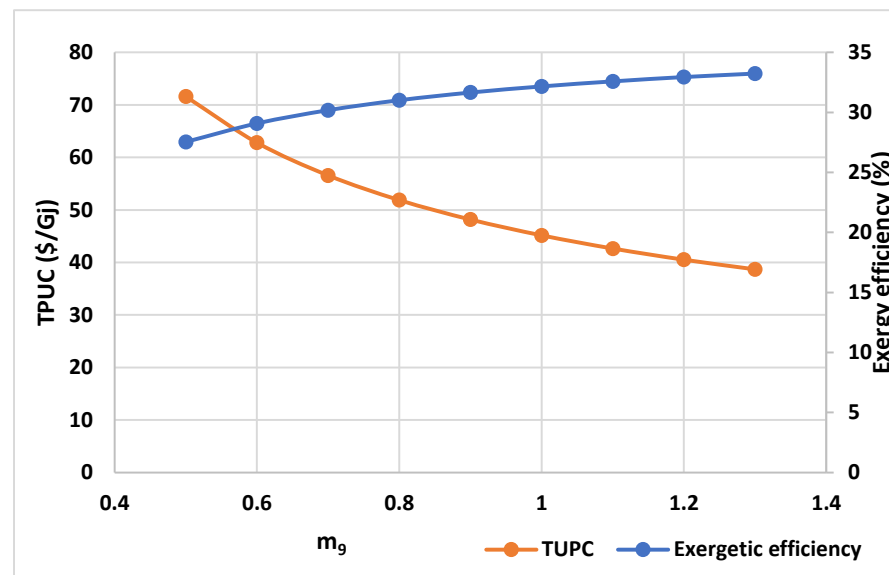
It should be observed that when the turbine inlet pressure increases, so does the total product unit cost. The finding makes sense, since as turbine inlet pressure rises, so does pump power. Nonetheless, increasing the input turbine pressure from 17,500 kPa to 22,000 kPa reduces cooling production from 274 kW to 272.4 kW while increasing generated power from 497.1 kW to 533.6 kW. Furthermore, the energy efficiency reaches a maximum of 15.78% at a pressure of 20,000 kPa, the exergy efficiency falls from 31.97% to 26.87%, and the total product unit cost climbs from 46.78 USD/GJ to 61.96 USD/GJ.

Figure 12a,b depict the effect of the secondary mass flow rate of the first ejector \dot{m}_9 on the thermodynamic and exergoeconomic system performance. The entrainment ratio was set. According to this figure, the rate of cooling and power generation increases while the rate of energy efficiency declines. Furthermore, exergy efficiency rises while total product unit cost falls. In other words, an increase in the first ejector’s secondary mass flow rate could result in a rise in the obtained refrigerant mass flow rate entering the turbine, \dot{m}_2 . As a result, the heating capacity of the steam generator increases while the energy efficiency drops. Furthermore, when exergy efficiency increases, so does the overall product unit cost. They vary in inverse proportion. At $\dot{m}_9 = 1.3$ kg/s, the exergetic efficiency achieved a maximum and the total product unit cost reached a minimum.



(a)

Figure 12. Cont.



(b)

Figure 12. (a) Effect of secondary mass flow rate of the first ejector on energy efficiency, cooling, and power generation. (b) Effect of the secondary mass flow rate of the first ejector on exergy efficiency and TPUC.

Nonetheless, increasing the secondary mass flow rate of the first ejector \dot{m}_9 from 0.5 kg/s to 1.3 kg/s increases cooling production from 212.4 kW to 335.2 kW and generated power from 259.7 kW to 745 kW. Furthermore, energy efficiency decreases from 18% to 14.78%, exergy efficiency increases from 27.54% to 33.23%, and total product unit cost drops from 71.58 USD/GJ to 38.69 USD/GJ.

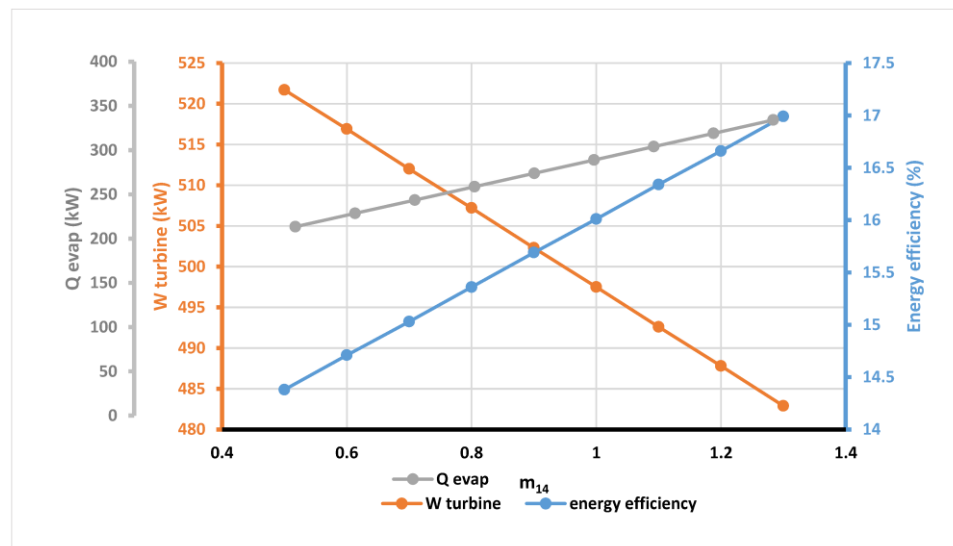
The behavior of the system's performance indicators against the secondary mass flow rate of the second ejector \dot{m}_{14} is depicted in Figure 13a,b. The second ejector's entrainment ratio was fixed. Figure 14 shows that the power generation rate decreases while the cooling production rate increases. Similarly, energy efficiency increases but exergy efficiency declines marginally. Furthermore, the overall product unit cost of products rises.

Increasing the secondary mass flow rate of the second ejector would increase the main mass flow rate \dot{m}_{13} . As a result, the outlet turbine mass flow rate \dot{m}_{10} would fall, resulting in a decrease in turbine power generation. However, the rise in energy efficiency is related to an increase in the cooling generation rate, which compensates for the reduced power production. Furthermore, as the exergy efficiency decreases, the overall product unit cost rises. They vary in inverse proportion. At a minimum value of the secondary mass flow rate of the second ejector, $\dot{m}_{14} = 0.5$ kg/s, the best exergetic efficiency, and the lowest total product unit cost are achieved.

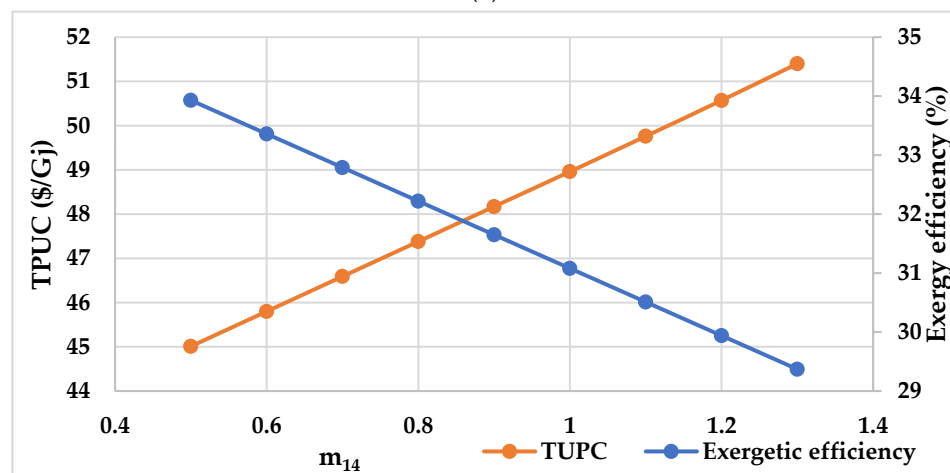
As illustrated in Figure 13, increasing the secondary mass flow rate of the first ejector \dot{m}_{14} from 0.5 kg/s to 1.3 kg/s improves the cooling output capacity from 213.5 kW to 334.1 kW. Furthermore, the power generation rate falls from 521.7 kW to 482.9 kW. The energy efficiency rises from 14.38% to 16.99%, whereas the exergy efficiency falls. Finally, the total unit cost of the product rises from 45.01 USD/GJ to 51.4 USD/GJ.

The effect of the extraction ratio on the thermodynamic and economic performance parameters tested in this study is depicted in Figure 14. This extraction ratio has a substantial impact on cycle performance. In terms of this figure, increasing this ratio reduces turbine power production while maintaining the cooling generation rate constant. Furthermore, energy efficiency improves, the exergy efficiency improves, and the total product unit cost rises. Indeed, increasing the extraction ratio could reduce the mass flow rate entering the turbine, \dot{m}_2 , as well as the heat power of the steam generator. As a result, turbine power generation is reduced while energy efficiency is raised. The exergy efficiency decreases because the quality of the electricity generated has the biggest effect on it. Therefore, a

decrease in the energy efficiency rate is associated with an increase in the overall product unit cost.



(a)

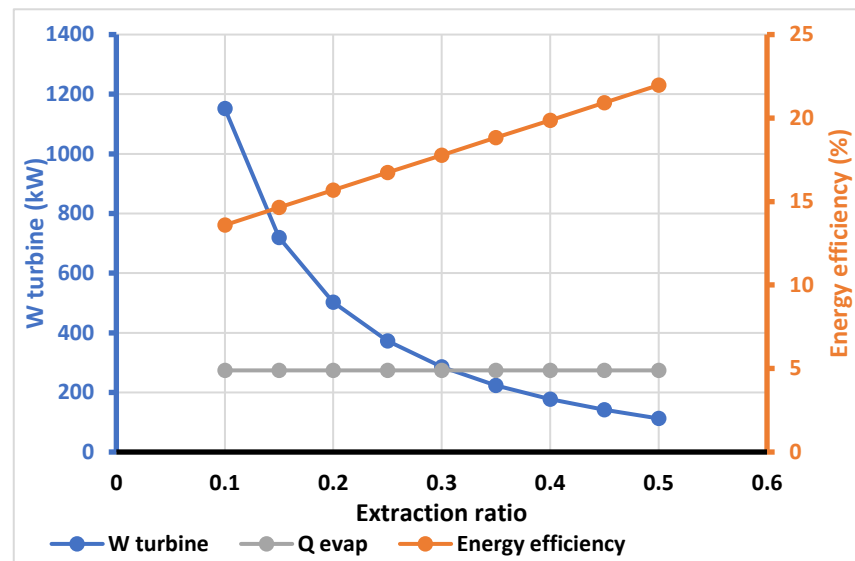


(b)

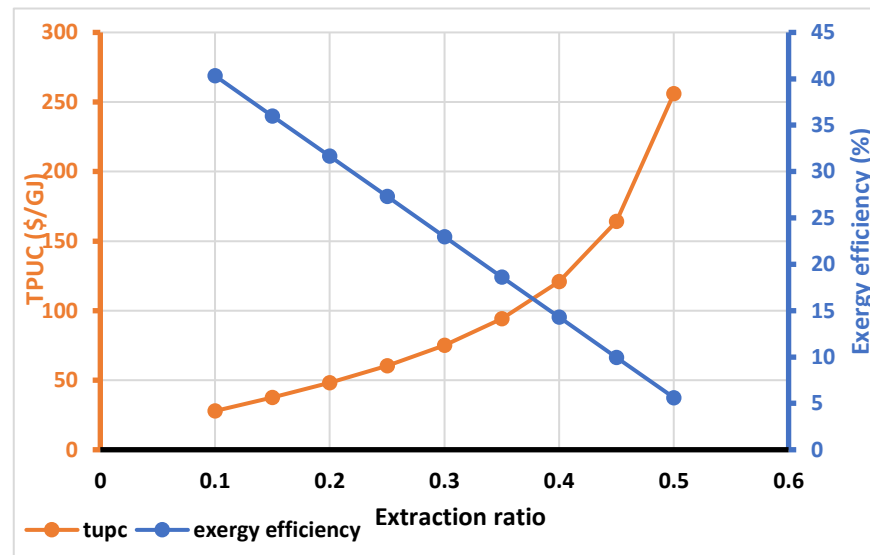
Figure 13. (a) Effect of the secondary mass flow rate of the second ejector on energy efficiency, cooling, and power generation. (b) Effect of the secondary mass flow rate of the second ejector on exergy efficiency and TPUC.

As seen in Figure 14, when the extraction ratio rises from 0.1 to 0.5, the rate of power production falls from 1152 kW to 112.5 kW, while the capacity of cooling production remains constant at 273.8 kW. When it comes to energy efficiency, it rises from 13.59% to 21.97% while falling from 40.33% to 5.6%. Finally, the cost of the entire product unit rises from 27.85 USD/GJ to 256.1 USD/GJ.

The parameter's effect on the system's thermodynamic and exergoeconomic performance was investigated. The total product unit cost, energy, exergy efficiency, turbine power output, cooling generation rate, and total product unit cost were all evaluated. However, parametric analysis is insufficient to determine the best design parameters. As a result, multi-objective optimization should be performed to establish the optimal system design parameters.



(a)



(b)

Figure 14. (a) Effect of the extraction ratio on energy efficiency, cooling, and power generation. (b) Effect of the extraction ratio on exergy efficiency and TPUC.

10. Optimization Results

The objective functions for the multi-objective optimization problem are exergy efficiency and total product unit cost. The simulation results are displayed graphically as curves or numerically as values. Figure 15 depicts the curves presented at the end of the simulation. They are as follows, from left to right and top to bottom:

- Dispersions among individuals of the same generation.
- Individual genealogy: the red, blue, and black lines represent the children of a mutation, a crossover, or elite, respectively.
- A histogram of the values assigned by the objective functions for each generation,
- The parents' histogram, which contributed to the construction of succeeding generations.
- The progression of the simulation's stopping criterion.
- The front or diagram of Pareto.
- The dispersion between the individuals constituting the Pareto.

- The rank of the individuals resulting from the simulation. The individuals of rank 1 constitute the Pareto front.
- The average variations measured in the differences between individuals from one generation to the next.

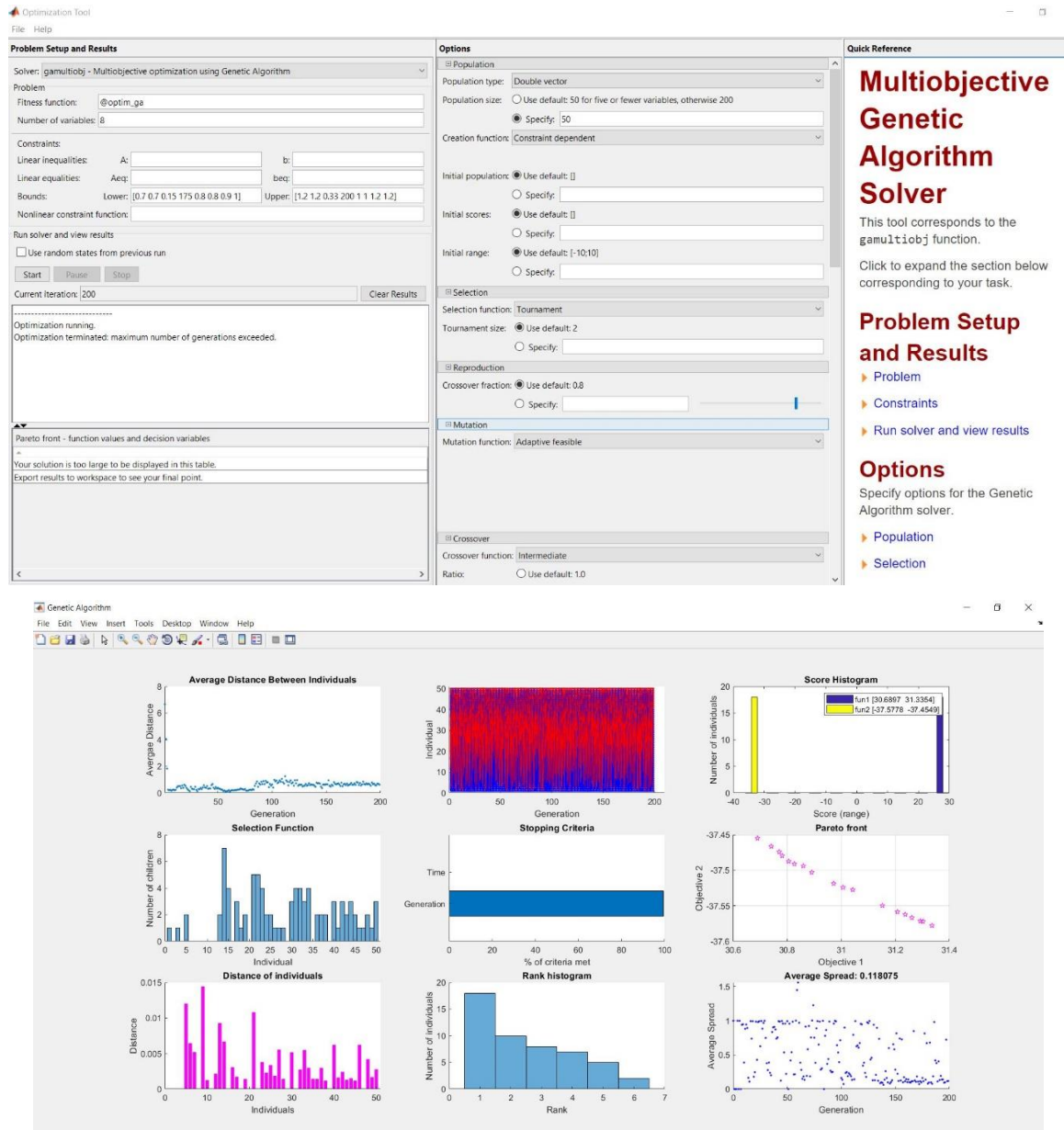


Figure 15. MATLAB simulation results.

Similarly, Figure 16 depicts the Pareto frontier determined using the MATLAB optimization program.

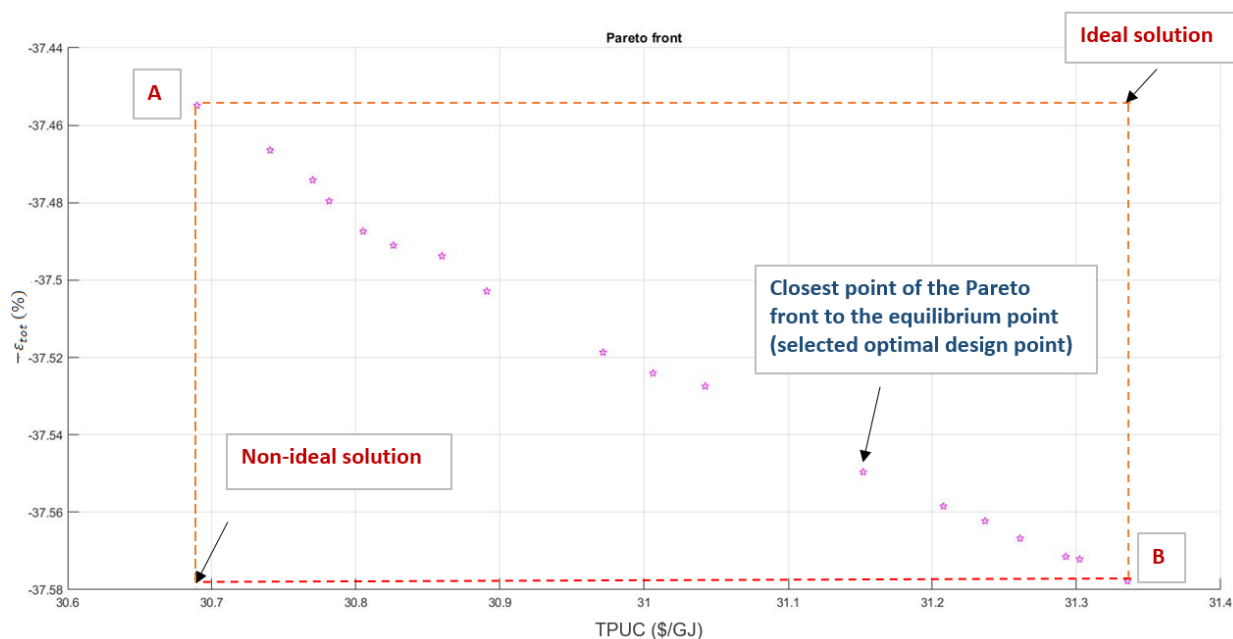


Figure 16. Pareto optimal solutions of the system’s TPUC and for exergy efficiency.

This graphic depicts the highest exergy efficiency (point B) and the lowest overall product unit cost (point A). This figure also illustrates the ideal and non-ideal solutions, as well as the optimal option. It should be noted that an exergy efficiency of 37.58% was recorded at design point B, with the TPUC reaching a maximum of 31.34 USD/GJ. Point A, on the other hand, had the lowest TPUC value of 30.69 USD/GJ and the lowest exergetic efficiency of 37.45%. If the TPUC or exergy efficiency is the only objective function, point A or B is deemed the ideal position. In the case of multi-objective optimization, the points on the Pareto frontier could be considered the best optimum option. The equilibrium ideal point, defined as the point at which both objective functions have their optimal value at the same time, was used in this work to determine the final optimum position. As seen in Figure 16, as the point approaches the Pareto frontier’s equilibrium point, it can be called the final optimum point. The TPUC and exergy efficiency are, respectively, 31.15 USD/GJ and 37.55%. Table 14 shows the values of the selected optimal solution and optimal design parameters. Furthermore, a comparison of the CMCP system’s base case and ideal case performance was performed (Table 15).

According to this table, the cooling and power generation rates will increase from 273.7 kW to 289.7 kW and 222.1 kW to 480 kW, respectively. Since the steam generator heat increased, energy efficiency decreased slightly, and overall exergy destruction increased. The rate of destruction lowered.

Table 14. Selected optimal solution.

Exergy Efficiency (%)	Cost of the Product (USD/Gj)	Secondary Mass Flow Rate \dot{m}_9	Secondary Mass Flow Rate \dot{m}_{14}	Extraction Ratio	Steam Generator Pressure (bar)	Evaporator 1 Coefficient $\text{kWm}^{-2}\text{K}^{-1}$	Evaporator 2 Coefficient $\text{kWm}^{-2}\text{K}^{-1}$	Condenser Coefficient $\text{kWm}^{-2}\text{K}^{-1}$	Steam Generator Coefficient $\text{kWm}^{-2}\text{K}^{-1}$
37.55	31.15	1.2	0.7	0.15	180.6	0.92	0.92	1.03	1.16

Table 15. Comparison between optimal case and base case.

Design Parameters	Base Case	Optimal Solution
Extraction ratio	0.2	0.15
Steam generator pressure (kPa)	18,000	18,060
Secondary mass flow rate \dot{m}_9	0.9	1.2
Secondary mass flow rate \dot{m}_{14}	0.9	0.7
Evaporator 1 coefficient	0.9	0.92
Evaporator 2 coefficient	0.9	0.92
Condenser coefficient	1	1.03
Steam generator coefficient	1	1.16
Energy efficiency	15.68	13.7
Evaporator cooling capacities Q_{tot} (kW)	273.7	289.77
Net power output (kW)	222.1	480
Steam generator heat (kW)	3161.9	5610.4
Total exergy destruction (kW)	459.6	756.7
Destruction cost rate $\dot{C}_{D,tot}$ (USD/h)	1.94	1.8
Total exergy efficiency (%)	31.64	37.55
Total product unit cost (USD/GJ)	48.38	31.15

11. Conclusions

In this work, multi-objective optimization and exergoeconomic analyses of a new combined multi-cooling and power generation system driven by solar energy are presented. The system includes a supercritical CO₂ power system for power generation and an ejector refrigeration system with two ejectors to provide cooling at two different evaporating temperatures. The PTC is used as the thermal energy source. The daily dynamic simulation of the source heat system was performed. The simulation hourly results of the temperature of the heat transfer fluid were used as input for the cogeneration system to estimate its performance. Exergy and energy analyses were performed to estimate the thermodynamic enhancement of the proposed system. Economic and exergoeconomic analyses were conducted to assess and optimize the system's cost. A thermodynamic parametric analysis of the system was carried out in line with an exergoeconomic study. It was found that increasing the turbine inlet pressure would enhance both the power generation and the TPUC. Furthermore, it was found that the system performance was significantly impacted by the turbine extraction ratio. It was discovered that power generation and energy efficiency decreased when the turbine extraction ratio rose.

A multi-objective optimization using a genetic algorithm with the total product unit cost and exergy efficiency as the objective functions determined the system's optimal conditions and design parameters. The thermodynamic model was solved by MATLAB software using the NIST database with the REFRPOP program to evaluate the refrigerant CO₂ thermodynamic properties. It was found that the highest amount of exergy destruction was for the ejector and the turbine. The multi-objective optimization showed that the turbine's extraction ratio, inlet pressure, and the ejector's secondary mass flow rate highly affected the power output of the turbine, cooling capacity, exergetic efficiency, and the TPUC. The optimal solution and design parameters of the system were determined with an exergy efficiency of 37.55% and TPUC of 31.15 USD/GJ.

Author Contributions: Conceptualization, R.H. and M.E.; Methodology, R.H.; Software, R.H.; Validation, M.E., B.T. and E.N.; Formal analysis, R.H.; Investigation, M.E.; Resources, M.E. and B.T.; Writing—original draft, R.H.; Writing—review & editing, M.E. and B.T.; Visualization, E.N.; Supervision, E.N. All authors have read and agreed to the published version of the manuscript.

Funding: This research received no external funding.

Data Availability Statement: The data that support the findings of this study are available on request from the corresponding author.

Conflicts of Interest: The authors declare no conflict of interest.

Nomenclature

Symbols

A	Surface per unit length (m)
BB	Expansion ratio of the turbine
\dot{C}	Cost rate (USD/h)
C	Factor of concentration
C_p	Gas-specific heat at constant pressure, ($\text{kJ kg}^{-1} \text{K}^{-1}$)
c	Specific exergy cost rate [USD/GJ]
c_F	Specific heat of the heat transfer fluid (kJ/kg K)
D	Diameter (m)
d	Diverging outlet section diameter of the nozzle motor (m)
d_D	Secondary nozzle diverging diameter (m)
d_*	Nozzle motor diameter (m)
\dot{E}	Exergy (kW)
e	Specific exergy (kJ/kg)
F_{BM}	Module factor
f_k	The exergoeconomic factor
G_i	The solar global irradiance (kW/m^2)
h	The enthalpy (kJ kg^{-1})
h_F	Convection heat transfer coefficient of the heat transfer fluid
i_{eff}	Rate of interest
k	Specific heat ratio (C_p/C_v)
I_G	The solar direct radiation (kW/m^2)
M	Mach number
\dot{m}	Mass flow rate (kg s^{-1})
n	Lifetime plant
P	Pressure
Q	Heat quantity (kJ)
\dot{Q}	Heat load (kW)
S	The entropy (kJ/kg K)
r	The ejector compression ratio
r_{OMC}	The average inflation rate of the operating and maintenance cost
r_{FC}	The average inflation rate of the fuel cost
r_k	The relative cost difference
T	Temperature
t	Time (s)
U	The ejector entrainment ratio
\dot{W}	Mechanical work (kW)
W_{eff}	Collector aperture (m)
X	Driving nozzle position about the throat of the mixer (m)
y^*	Exergy destruction ratio
Z	Distance (m)
\dot{Z}	The components' cost rate [USD/h]
\dot{Z}_{tot}	Total system cost rate [USD/h]

Abbreviations

BMC	Bare module cost
CMCP	Combined multi-cooling and power generation
CEPCI	Chemical engineering plant cost index
CRF	Capital recovery factor
CELF	Constant escalation levelization factor
CC	Carrying charges
ECC	Ejector cooling cycle
FCI	Fixed capital investment
FC	Fuel cost
GA	Genetic Algorithm
HTF	Heat Transfer Fluid

ORC	Organic Rankine Cycle
OMC	Operating and maintenance cost
ROI	Return on investment
PEC	Purchased equipment cost
PTC	Parabolic Trough Collector
X	Size of equipment
TCI	Total capital investment
TPUC	Total product unit cost
TRR	Total Revenue Requirement
Greek letters	
ρ	Reflectivity
ρ_A	The density of the absorber pipe (kg/m ³)
ρ_F	The density of fluid (kg/m ³)
β	Inclination angle
α	Thermal diffusivity
$\gamma_{\text{interception}}$	Factor of interception
η	Efficiency
τ	The mirror's transmittance
Δ	Related to the variation of a parameter
Φ	Ejector geometrical ratio
θ	Temperature ratio (T'' / T')
Γ	The expansion ratio
ξ	The driving pressure ratio
Ω	The ratio of the outlet section of the nozzle on the side of the mixing chamber
η	Energy efficiency
ε	Exergy efficiency
τ	Full load operational time
Exponents and Subscripts	
A	Absorber pipe
abs	Absorbed
amb	Ambient
ch	Chemical
D	Destruct
e1	Evaporator 1
e2	Evaporator 2
ev1	Expansion valve 1
ev2	Expansion valve 2
ejec1	Ejector 1
ejec2	Ejector 2
ext	External
F	Fluid
F	Fuel (exergy fuel)
Ger	Steam generator
L	Loss
l	Levelized
int	Internal
in	Entry
kn	Kinetic
Known	Known equipment
Net	Net
New	New equipment
Out	Outlet
Old	The year the equipment's cost was valid
p	Product
p1,p2,p3	Pump 1,2,3
ph	Physical
pt	Potential

Ref	The year it was intended to be acquired
turb	Turbine
i	Given state
0	reference state (for exergy analysis)
1,2,3	Cycle locations
k	kth component
tot	Total
V	The glass envelope
*	Fluid critical state
'	High-pressure working fluid
"	Entrained low-pressure fluid

References

1. IEA—International Energy Agency. Key World Energy Statistics. 2017. Available online: <http://www.iea.org/statistics/> (accessed on 1 November 2022).
2. Jamali, A.; Ahmadi, P.; Mohd, J.; Mohammad, N. Optimization of a novel carbon dioxide cogeneration system using artificial neural network and multi-objective genetic algorithm. *Appl. Therm. Eng.* **2014**, *64*, 293–306. [CrossRef]
3. Kong, X.; Wang, R.; Huang, X. Energy efficiency and economic feasibility of CCHP driven by stirling engine. *Energy Convers. Manag.* **2004**, *45*, 1433–1442. [CrossRef]
4. White, M.T.; Bianchi, G.; Chai, L.; Tassou, S.A.; Sayma, A.I. Review of supercritical CO₂ technologies and systems for power generation. *Appl. Therm. Eng.* **2020**, *185*, 116447. [CrossRef]
5. Tchanche, B.F.; Lambrinos, G.; Frangoudakis, A.; Papadakis, G. Low-grade heat conversion into power using organic Rankine cycles—A review of various applications. *Renew. Sustain. Energy Rev.* **2011**, *15*, 3963–3979. [CrossRef]
6. Qiu, G.; Shao, Y.; Li, J.; Liu, H.; Riffat, S.B. Experimental investigation of a biomass-fired ORC-based micro-CHP for domestic applications. *Fuel* **2012**, *96*, 374–382. [CrossRef]
7. DiPippo, R. Geothermal power plants: Evolution and performance assessments. *Geothermics* **2015**, *53*, 291–307. [CrossRef]
8. Uehara, H.; Dilao, C.O.; Nakaoka, T. Conceptual design of ocean thermal energy conversion (OTEC) power plants in the Philippines. *Sol. Energy* **1988**, 41431–41441. [CrossRef]
9. García, R.L.; Peñate, B. Seawater reverse osmosis desalination driven by a solar Organic Rankine Cycle: Design and technology assessment for medium capacity range. *Desalination* **2012**, *284*, 86–91.
10. Shi, L.; Shu, G.; Tian, H.; Deng, S. A review of modified Organic Rankine cycles (ORCs) for internal combustion engine waste heat recovery (ICE-WHR). *Renew. Sustain. Energy Rev.* **2018**, *92*, 95–110. [CrossRef]
11. Xu, B.; Rathod, D.; Yebi, A.; Filipi, Z.; Onori, S.; Hoffman, M. A comprehensive review of organic Rankine cycle waste heat recovery systems in heavy-duty diesel engine applications. *Renew. Sustain. Energy Rev.* **2019**, *107*, 145–170. [CrossRef]
12. Mago, P.J.; Hueffed, A.; Chamra, L.M. Analysis and optimization of the use of CHP–ORC systems for small commercial buildings. *Energy Build.* **2010**, *42*, 1491–1498. [CrossRef]
13. Wei, Y.; Huitao, W.; Zhong, G. Comprehensive analysis of a novel power and cooling cogeneration system based on organic Rankine cycle and ejector refrigeration cycle. *Energy Convers. Manag.* **2021**, *232*, 113898.
14. Wu, D.; Wang, R. Combined cooling, heating and power: A review. *Prog. Energy Combust. Sci.* **2006**, *32*, 459–495. [CrossRef]
15. Dai, Y.; Wang, J.; Gao, L. Exergy analysis, parametric analysis and optimization for a novel combined power and ejector refrigeration cycle. *Appl. Therm. Eng.* **2009**, *29*, 1983–1990. [CrossRef]
16. Liu, Z.; Liu, Z.; Cao, X.; Li, H.; Yang, X. Self-condensing transcritical CO₂ cogeneration system with extraction turbine and ejector refrigeration cycle: A techno-economic assessment study. *Energy* **2020**, *208*, 118391. [CrossRef]
17. Ayou, D.S.; Bruno, J.C.; Saravanan, R.; Coronas, A. An overview of combined absorption power and cooling cycles. *Renew. Sustain. Energy Rev.* **2013**, *21*, 728–748. [CrossRef]
18. Yogi, G.D.; Feng, X. Analysis of a new thermodynamic cycle for combined power and cooling using low and mid temperature solar collectors. *J. Sol. Energy Eng.* **1999**, *121*, 91–97.
19. Ghaebi, H.; Parikhani, T.; Rostamzadeh, H.; Farhang, B. Thermodynamic and thermoeconomic analysis and optimization of a novel combined cooling and power (CCP) cycle by integrating of ejector refrigeration and Kalina cycles. *Energy* **2017**, *139*, 262–276. [CrossRef]
20. Tashtoush, B.; Nayfeh, Y. Energy and economic analysis of a variable-geometry ejector in solar cooling systems for residential buildings. *J. Energy Storage* **2020**, *27*, 101061. [CrossRef]
21. Elakhdar, M.; Nehdi, E.; Kairouani, L. Thermodynamic analysis of a novel Ejector Enhanced Vapor Compression Refrigeration (EEVCR) cycle. *Energy* **2018**, *163*, 1217–1230. [CrossRef]
22. Tashtoush, B.; Younes, M.B. Comparative Thermodynamic Study of Refrigerants to Select the Best Environment-Friendly Refrigerant for Use in a Solar Ejector Cooling System. *Arab. J. Sci. Eng.* **2019**, *44*, 1165–1184. [CrossRef]
23. Megdoul, K.; Tashtoush, B.; Nahdi, E.; Elakhdar, M.; Kairouani, L.; Mhimid, A. Thermodynamic analysis of a novel ejector-cascade refrigeration cycles for freezing process applications and air-conditioning. *Int. J. Refrig.* **2016**, *70*, 108–118. [CrossRef]

24. Wang, M.; Wang, J.; Zhao, P.; Dai, Y. Multi-objective optimization of a combined cooling, heating and power system driven by solar energy. *Energy Convers. Manag.* **2015**, *89*, 289–297. [[CrossRef](#)]
25. Wang, J.; Dai, Y.; Sun, Z.A. Theoretical study on a novel combined power and ejector refrigeration cycle. *Int. J. Refrig.* **2009**, *32*, 1186–1194. [[CrossRef](#)]
26. Zheng, B.; Weng, Y.W. A combined power and ejector refrigeration cycle for low temperature heat sources. *Sol. Energy* **2010**, *84*, 779–784. [[CrossRef](#)]
27. Wang, J.; Zhao, P.; Niu, X.; Dai, Y. Parametric analysis of a new combined cooling, heating and power system with transcritical CO₂ driven by solar energy. *Appl. Energy* **2012**, *94*, 58–64. [[CrossRef](#)]
28. Habibzadeh, A.; Rashidi, M.M.; Galanis, N. Analysis of a combined power and ejector-refrigeration cycle using low temperature heat. *Energy Convers. Manag.* **2013**, *65*, 381–391. [[CrossRef](#)]
29. Landoulsi, H.; Elakhdar, M.; Nehdi, E.; Kairouani, L. Performance analysis of a combined system for cold and power. *Int. J. Refrig.* **2015**, *60*, 297–308. [[CrossRef](#)]
30. Rostamzadeh, H.; Ghaebi, H.; Parikhani, T. Thermodynamic and thermoeconomic analysis of a novel combined cooling and power (CCP) cycle. *Appl. Therm. Eng.* **2018**, *139*, 474–487. [[CrossRef](#)]
31. Behnam, P.; Faegh, M.; Shafii, M.B. Thermodynamic analysis of a novel combined power and refrigeration cycle comprising of Kalina and ejector refrigeration cycles. *Int. J. Refrig.* **2019**, *104*, 291–301. [[CrossRef](#)]
32. Rostamzadeh, H.; Ghaebi, H.; Behnam, F. Energetic and exergetic analyses of modified combined power and ejector refrigeration cycles. *Therm. Sci. Eng. Prog.* **2017**, *2*, 119–139. [[CrossRef](#)]
33. Mehrpooya, M.; Tosang, E.; Dadak, A. Investigation of a combined cycle power plant coupled with a parabolic trough solar field and high temperature energy storage system. *Energy Convers. Manag.* **2018**, *171*, 1662–1674. [[CrossRef](#)]
34. Haghghi, M.A.; Mohammadi, Z.; Pesteei, S.M.; Chitsaz, A.; Parham, K. Exergoeconomic evaluation of a system driven by parabolic trough solar collectors for combined cooling, heating, and power generation; a case study. *Energy* **2019**, *192*, 116594. [[CrossRef](#)]
35. Wang, J.; Yan, Z.; Wang, M.; Li, M.; Dai, Y. Multi-objective optimization of an organic Rankine cycle (ORC) for low grade waste heat recovery using evolutionary algorithm. *Energy Convers. Manag.* **2013**, *71*, 146–158. [[CrossRef](#)]
36. Pierobon, L.; Nguyen, T.-V.; Larsen, U.; Haglind, F.; Elmegaard, B. Multi-objective optimization of organic Rankine cycles for waste heat recovery: Application in an offshore platform. *Energy* **2013**, *58*, 538–549. [[CrossRef](#)]
37. Yao, E.; Wang, H.; Wang, L.; Xi, G.; Maréchal, F. Multi-objective optimization and exergoeconomic analysis of a combined cooling, heating and power based compressed air energy storage system. *Energy Convers. Manag.* **2017**, *138*, 199–209. [[CrossRef](#)]
38. Ahmadzadeh, A.; Salimpour, M.R.; Sedaghat, A. Thermal and exergoeconomic analysis of a novel solar driven combined power and ejector refrigeration (CPEER) system. *Int. J. Refrig.* **2017**, *83*, 143–156. [[CrossRef](#)]
39. Moghimi, M.; Emadi, M.; Ahmadi, P.; Moghadasi, H. 4E analysis and multi-objective optimization of a CCHP cycle based on gas turbine and ejector refrigeration. *Appl. Therm. Eng.* **2018**, *141*, 516–530. [[CrossRef](#)]
40. Sadeghi, M.; Mahmoudi SM, S.; Khoshbakhti Saray, R. Exergoeconomic analysis and multi-objective optimization of an ejector refrigeration cycle powered by an internal combustion (HCCI) engine. *Energy Convers. Manag.* **2015**, *96*, 403–417. [[CrossRef](#)]
41. Sanaye, S.; Refahi, A. A novel configuration of ejector refrigeration cycle coupled with organic Rankine cycle for transformer and space cooling applications. *Int. J. Refrig.* **2020**, *115*, 191–208. [[CrossRef](#)]
42. Roupedakis, T.C.; Loumpardis, G.; Monokrousou, E.; Braimakis, K.; Charalampidis, A.; Karellas, S. Exergetic and economic analysis of a solar driven small scale ORC. *Renew. Energy* **2020**, *157*, 1008–1024. [[CrossRef](#)]
43. Mouna, E.; Hanene, L.; Bourhan, T.; Ezzedine, N.; Lakdar, K. A combined thermal system of ejector refrigeration and Organic Rankine cycles for power generation using a solar parabolic trough. *Energy Convers. Manag.* **2019**, *199*, 111947. [[CrossRef](#)]
44. Moussawi, H.A.; Fardoun, F.; Louahlia, H. Selection based on differences between cogeneration and trigeneration in various prime mover technologies. *Renew. Sustain. Energy Rev.* **2017**, *74*, 491–511. [[CrossRef](#)]
45. Dostal, V.; Hejzlar, P.; Driscoll, M.J. The Supercritical Carbon Dioxide Power Cycle: Comparison to Other Advanced Power Cycles. *Nucl. Technol.* **2006**, *154*, 283–301. [[CrossRef](#)]
46. Lu, M.T.; Milani, D.; McNaughton, R.; Abbas, A. Analysis for flexible operation of supercritical CO₂ Brayton cycle integrated with solar thermal systems. *Energy* **2017**, *124*, 752–771. [[CrossRef](#)]
47. Zhou, T.L.; Li, X.; Zhao, M.; Zhao, Y. Thermodynamic design space data-mining and multi-objective optimization of SCO₂ Brayton cycles. *Energy Convers. Manage.* **2021**, *249*, 114844. [[CrossRef](#)]
48. Ahn, Y.; Bae, S.J.; Kim, M.; Cho, S.K.; Baik, S.; Lee, J.I.; Cha, J.E. Review of supercritical CO₂ power cycle technology and current status of research and development. *Nucl. Eng. Technol.* **2015**, *47*, 647–661. [[CrossRef](#)]
49. Li, M.J.; Zhu, H.H.; Guo, J.Q.; Wang, K.; Tao, W.Q. The development technology and applications of supercritical CO₂ power cycle in nuclear energy, solar energy and other energy industries. *Appl. Therm. Eng.* **2017**, *126*, 255–275. [[CrossRef](#)]
50. Yulei, H.; Peixue, J.; Yin Hai, Z. Analysis of a novel combined cooling and power system by integrating of supercritical CO₂ Brayton cycle and transcritical ejector refrigeration cycle. *Energy Convers. Manag.* **2022**, *269*, 116081.
51. Lykas, P.; Georgousis, N.; Bellos, E.; Tzivanidis, C. Multi-objective optimization of combined cooling, heating, and power systems with supercritical CO₂ recompression Brayton cycle. *Appl. Energy* **2022**, *311*, 118717. [[CrossRef](#)]
52. Kalogirou, S. Solar thermal collectors and application. *Energy Combust. Sci.* **2004**, *30*, 31–295. [[CrossRef](#)]

53. Huang, B.J.; Chang, J.M.; Wang, C.P.; Petrenko, V.A. A 1-D analysis of ejector performance. *Int. J. Refrig.* **1999**, *22*, 354–364. [[CrossRef](#)]
54. Zhu, Y.; Cai, W.; Wen, C.; Li, Y. Shock circle model for ejector performance evaluation. *Energy Convers. Manage.* **2007**, *48*, 2533–2541. [[CrossRef](#)]
55. Elakhdar, M.; Nehdi, E.; Kairouani, L.; Tounsi, N. Simulation of an ejector used in refrigeration systems. *Int. J. Refrig.* **2011**, *34*, 1657–1667. [[CrossRef](#)]
56. Lu, L.T. Etudes théorique et expérimentale de la production de froid par machine tritherme a éjecteur de fluide frigorigène. Ph.D. Thesis, Laboratoire d’Energétique et d’Automatique, de l’INSA de Lyon, Lyon, France, 1986.
57. Nahdi, E.; Champoussin, J.C.; Hostache, G.; Cheron, J. Optimal geometric parameters of a cooling ejector-compressor. *Int. J. Refrig.* **1993**, *16*, 67–72. [[CrossRef](#)]
58. Bejan, A.; Tsatsaronis, G. *Thermal Design and Optimization*; John Wiley & Sons: Hoboken, NJ, USA, 1996; p. 9.
59. Tashtoush, B.; Morosuk, T.; Chudasama, J. Exergy and Exergoeconomic Analysis of a Cogeneration Hybrid Solar Organic Rankine Cycle with Ejector. *Entropy* **2020**, *22*, 702. [[CrossRef](#)] [[PubMed](#)]
60. Holland, J.H. *Adaptation in Natural and Artificial Systems: An Introductory Analysis with Applications to Biology, Control, and Artificial Intelligence*; U Michigan Press; MIT Press: Cambridge, MA, USA, 1975.
61. Kalyanmoy, D. *Multi-Objective Optimization Using Evolutionary Algorithms*; John Wiley & Sons, Ltd.: Chichester, UK, 2001.
62. Mathworks. Available online: <https://www.mathworks.com/help/gads/gamultiobj-algorithm.html#brjtxfv-1> (accessed on 19 January 2023).
63. Nehdi, E.; Kairouani, L.; Elakhdar, M. A solar ejector air-conditioning system using environment-friendly working fluids. *Int. J. Energy Res.* **2008**, *32*, 1194–1201. [[CrossRef](#)]
64. Dorantes, R.; Lallemand, A. Influence de la nature des fluides, purs ou en mélange non-azéotropiques, sur les performances d’une machine de climatisation a ejecto compresseur. *Int. J. Refrig.* **1995**, *18*, 21–30. [[CrossRef](#)]
65. Balgouthi, M.; Hadj Ali, A.; Trabelsi, S.; Guizani, A. Optical and thermal evaluations of a medium temperature parabolic trough solar collector used in a cooling installation. *Energy Convers. Manage.* **2014**, *86*, 1134–1146. [[CrossRef](#)]
66. Lemmon, E.; McLinden, M.; Huber, M. *NIST Standard Reference Database 23: Reference Fluid Thermodynamic and Transport Properties-REFPROP, Version 9.0*; National Institute of Standards and Technology, Standard Reference Data Program: Gaithersburg, MD, USA, 2010.

Disclaimer/Publisher’s Note: The statements, opinions and data contained in all publications are solely those of the individual author(s) and contributor(s) and not of MDPI and/or the editor(s). MDPI and/or the editor(s) disclaim responsibility for any injury to people or property resulting from any ideas, methods, instructions or products referred to in the content.